

Analysis of a parametrically excited 2DOF oscillator with nonlinear restoring magnetic force and rotating rectangular beam

February 3, 2026

Muhammad Junaid-U-Rehman¹, Grzegorz Kudra^{1,*}, Krystian Polczyński¹, Kevin Dekemele², Jan Awrejcewicz¹

¹*Department of Automation, Biomechanics, and Mechatronics, Lodz University of Technology, 1/15 Stefanowski st., 90 – 537 Łódź, Poland*

²*Department of Electromechanical Systems and Metal Engineering, Ghent University, Technologiepark 46, Ghent, Belgium*

Abstract

This study investigates a detailed analytical and numerical investigation of a nonlinear two-degree-of-freedom (2DOF) mechanical oscillator subjected to parametric excitation, magnetic stiffness nonlinearities, and dry friction. The considered system consists of two coupled oscillators, both of which are connected to a rotating rectangular beam that induces a time-periodic stiffness variation. The Complex Averaging (CxA) method is employed to derive approximate analytical solutions, which are thoroughly validated through time-domain simulations and bifurcation analyses. The dynamic analysis reveals a rich spectrum of nonlinear behaviors, including periodic, quasi-periodic, and chaotic responses. Detailed bifurcation diagrams, Lyapunov exponent analysis, and Poincaré maps demonstrate the influence of nonlinear stiffness degree, mass symmetry, and frictional effects on system stability and response amplitude. The obtained results give a significant understanding of the dynamic behavior of coupled nonlinear systems and establish a conceptual framework for the development of complex vibration abatement strategies, energy harvesting devices, and advanced mechanical systems.

Keywords: Magnetic oscillators, Parametric excitation, Magnetic interaction, Complex Averaging Method, Variable stiffness

1 Introduction

The significance of differential equations (DEs) in science and engineering is paramount. They function as effective methods for modeling, evaluating, and estimating the behavior of dynamic systems across different areas of study. DEs provide a mathematical

E-mail address: (M. J. Rehman) muhammad-junaid.u-rehman@dokt.p.lodz.pl, (G. Kudra^{*}) grzegorz.kudra@p.lodz.pl, (K. Polczyński) krystian.polczynski@p.lodz.pl, (K. Dekemele) kevin.dekemele@ugent.be, (J. Awrejcewicz) jan.awrejcewicz@p.lodz.pl

framework for analyzing complex events, encouraging scientists and engineers to tackle significant problems, make informed decisions, and foster innovation and advancement in their respective fields. DEs are essential in engineering for the analysis and design of systems, including electrical circuits, mechanical structures, fluid flow systems, and control systems. DEs are utilized in mechanical engineering (ME) to analyze the dynamics of mechanical systems, such as vibrations, heat transfer, and fluid movement, allowing engineers to enhance designs for efficiency, safety, and performance. In electrical engineering (EE), DEs model the behavior of circuits comprising resistors, capacitors, and inductors, enabling engineers to predict voltage and current distributions and design circuits with specific features [1–5].

The study of mechanical oscillators, particularly those with multiple degrees of freedom (DOF), has been a fundamental area of research in the field of applied mechanics and engineering dynamics. Systems exhibiting parametric excitation and dry friction [6] forces are particularly challenging due to their complex, nonlinear behaviors, which include bifurcations and chaotic responses. Parametrically excited systems based on Mathieu-type equations have been studied extensively in the literature [7–9], often without considering dry friction effects. These systems serve as classical examples of parametric excitation, with their dynamic behavior thoroughly investigated in numerous scholarly works [10,11]. Understanding these dynamics is crucial for designing and optimizing mechanical systems used in various industries, including automotive, aerospace, and civil engineering. Examples of parametric oscillators in mechanical systems include pendulums with adjustable suspension points [12]. Such oscillations are observable in fundamental electrical systems [13], and we can also see the parametric excitation in molecular physics [14]. The stabilizing behavior of the inverted pendulum, as investigated by P. Kapitza [15], may resemble their behavior. A.H. Nayfeh discussed the 1DOF and 2DOF parametric oscillator by employing the multiple scales scheme and without dry friction in [16–18]. J. Awrejcewicz et al. discussed the nonlinear dynamics of the 2DOF spring pendulum encompassing resonant and non-resonant oscillations. The resonance curves have been developed, and a stability study has been conducted. The kinematically excited spring pendulum is examined using the three time scales of the method of multiple scales, and both parametric and primary resonances, occurring either concurrently or independently, are explored in [19].

Friction is a tangential reaction force that arises between two surfaces in contact and plays an important role in power transmission across a wide range of mechanical systems. It is present in nearly all mechanical engineering applications, including bearings, gear systems, hydraulic and pneumatic actuators, robotic joints, valves, disc brakes, and wheels. The phenomenon of friction stems from various underlying mechanisms, such as elastic and plastic deformation, fluid interactions, wave propagation, and material properties [20]. Due to its inherently nonlinear nature, friction can lead to complex behaviors such as steady-state errors, limit cycles, and degraded system performance. A more comprehensive elucidation of the friction phenomenon at low velocities, particularly during the transition through zero velocity, is essential. Karnopp presented a model to resolve issues related to zero velocity detection and to prevent transitions between distinct state equations for sticking and sliding in [21]. A large number of scientists and researchers examined the friction models. Filippov [22] examined the discontinuous dynamical characteristics of a Coulomb friction oscillator and introduced a DEs theory featuring discontinuous right-hand sides. The differential inclusion was introduced using set-valued analysis to describe sliding motion over the discontinuous border. Common instances include

various combinations of Coulomb friction, viscous friction, and the Stribeck effect [23]. Haessig and Friedland introduced a bristle model [24], while Coulomb, hyperbolic tangent, and LuGre were explained in [25]. Shaw [26] investigated the stability of periodic responses in friction-driven oscillators using Poincaré map techniques. In a related study, Awrejcewicz and Delfs [27] analyzed the equilibrium stability of a two-degree-of-freedom system influenced by dry friction. Feeny and Moon [28] explored the chaotic behavior of a dry-friction oscillator through both experimental observations and numerical simulations. Additionally, Oestreich et al. [29] studied the bifurcation characteristics and stability of a non-smooth oscillator subject to frictional effects. A classical model addressing certain dynamic friction phenomena was proposed by Armstrong in [30].

Damping has played a significant role in friction-induced vibrations. Hoffmann and Gaul [31] examined a mass-on-belt system via the lens of the mode-coupling mechanism, revealing that non-proportional damping may unexpectedly destabilize the system despite expectations to the contrary. Fritz and colleagues [32] employed an FEM of a whole braking corner, followed by a stability analysis, to investigate how damping influences the patterns of brake squeal coalescence. Sinou and Jezequel [33] made analogous observations, indicating that an optimal structural damping ratio and pulsation ratio can reduce the unstable zone caused by mode coupling. An experimental study on the correlation between modal damping distribution and the tendency to produce squeal in a beam-on-disk configuration was conducted by Massi and Giannini [34]. A mass-spring system that can move in three dimensions and includes friction, and they analyzed how different system parameters affect stability, especially looking at how damping affects instabilities when modes couple under flat and straight friction conditions, was discussed by Charroyer and colleagues [35]. In addition to damping, nonlinear contact stiffness has a significant influence on the identification of unstable zones. Li et al. [36] demonstrated that increasing the nonlinear stiffness generally leads to system destabilization; however, stability can be regained within certain higher stiffness ranges.

Typically, vibrations are considered unpleasant. Their impact on mechanical systems is detrimental and can lead to expensive malfunctions. In the last decades, there has been a growing focus on the movement of the nonlinear 2DOF oscillation system [37–39]. The behavior of interconnected vibrating systems, such as elastic beams supported by two springs and the vibration of a milling machine, can be accurately represented using these 2DOF systems [40]. Their equations of motion are comprised of two second-order differential equations that include cubic nonlinearities. The literature is described in standard vibration textbooks [41] and can also be found in References [42, 43]. M. Krack and J. Gross used the harmonic balance method for investigating nonlinear vibrations in mechanical systems and for identifying, analyzing, and controlling complex dynamical behaviors in engineering applications [44]. Furthermore, J. Awrejcewicz and collaborators explored system stability, bifurcations, and Lyapunov exponents using Floquet theory applied to damped Mathieu-type systems [45–47].

Considering the previous background, the goal of this research is to examine the different dynamics of a 2DOF parametric oscillator system subject to periodic variations in its parameters, resulting in rich dynamic behaviors. This study builds on previous works that have explored the dynamics of 1DOF systems [48, 49] but expands the analysis to 2DOF systems, which are more representative of real-world engineering applications. The main objective of this study is to explore and discuss the different dynamics by using the CxA method alongside numerical simulations to capture the intricate dynamics of the system. Utilizing a CxA method, we derive a series of modulation equations that are

readily interpretable in physical terms and provide insight into the amplitude-frequency response [50, 51]. We have computed the numerical results of the 2DOF parametric system, including time plots, phase plots, bifurcation diagrams for a deeper look at different dynamics, and Lyapunov exponents, which confirm the behavior of the considered system. By comparing analytical and numerical results, the research aims to bridge the gap between theoretical models and practical applications. The analysis will cover the influence of nonlinear stiffness and dry friction on the system's response, providing insights into how these factors contribute to the overall stability and performance of mechanical systems.

The research is structured as follows: Section 2 introduces the dynamical system, and it is divided into four further subsections: The physical model is described in detail in subsection 2.1; the mathematical model of the system and dimensional and nondimensional equations of motion are derived in subsections 2.2 and 2.3; and dimensional and nondimensional system parameters are examined in subsection 2.4. In Section 3, analytical solutions are computed by using the CxA method. Section 4 explores the amplitude frequency response by the CxA method, a comparison analysis of analytical and numerical results, bifurcation analysis, and time, phase, and Poincaré plots for the considered parametric system, and it is divided into two subsections; firstly, we investigated the 2DOF system with the different masses in subsection 4.1, and then we discussed the 2DOF system with the same masses in subsection 4.2. At last, Section 5 summarizes the results and conclusions of this investigation.

2 Dynamical System

2.1 Physical model

The physical concept of the investigated system is presented in Fig. 1. This is a physical model of a possible experimental setup that is an extension of the 1DOF system experimentally studied in the works [48, 49] to a 2DOF system.

The system consists of two bodies with masses m_1 and m_2 moving parallel on rolling guides, whose displacement relative to the equilibrium position is defined by coordinates x_1 and x_2 , respectively. The motion resistances, the main source of which are the rolling guides, are modeled as the sum of the viscous damping (with coefficients c_1 and c_2) and a component mathematically equivalent to the Coulomb dry friction (parameters T_1 and T_2). Each body features a strongly nonlinear spring realized by appropriate pairs of repulsive magnets, mounted so that in the equilibrium position the distance between them is δ_1 and δ_2 , respectively. Both bodies are coupled by an additional linear spring implemented utilizing a beam connecting them. This beam has a rectangular cross-section with dimensions a and b , so the spring has different stiffnesses in the two principal directions, equal to k_ξ and k_η , respectively. One of the bodies is equipped with a stepper motor that controls the angular position of the beam $\varphi(t)$. Presented studies assume a constant angular velocity of the beam, Ω , and angle $\varphi(t) = \Omega t$.

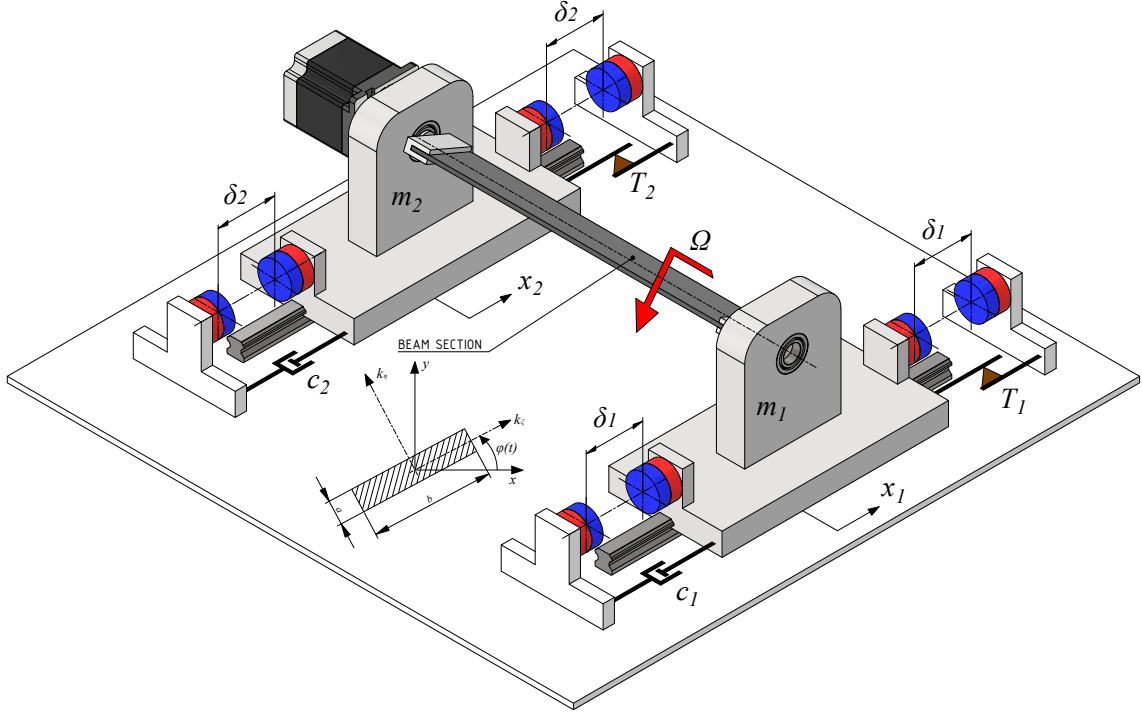


Figure 1: Experimental setup of 2DOF mechanical parametric oscillator.

2.2 Dimensional equations of motion

The physical model presented in the previous section is described by the following governing equations of motion:

$$\begin{aligned} m_1 \ddot{x}_1 + c_1 \dot{x}_1 + T_1 f_0(\dot{x}_1) + K(t)(x_1 - x_2) + F_{s1}(x_1) &= 0, \\ m_2 \ddot{x}_2 + c_2 \dot{x}_2 + T_2 f_0(\dot{x}_2) + K(t)(x_2 - x_1) + F_{s2}(x_2) &= 0. \end{aligned} \quad (1)$$

In the above equations, the terms $c_i \dot{x}_i + T_i f_0(\dot{x}_i)$; $i = 1, 2$, represent the resistance force in the rolling guide (for details, see [48]). The following set-valued function $f_0(v)$ is used to describe the Coulomb friction law

$$f_0(v) \begin{cases} = 1, & \text{if } v > 0, \\ \in [-1, 1], & \text{if } v = 0, \\ = -1, & \text{if } v < 0. \end{cases} \quad (2a)$$

$$(2b)$$

$$(2c)$$

The function $K(t) = \frac{k_\xi + k_\eta}{2} + \frac{k_\xi - k_\eta}{2} \cos(2\Omega t)$ represents the stiffness that varies over time due to the beam that connects the two oscillators and rotates at angular velocity Ω . The forces $F_{si}(x_i)$; $i = 1, 2$, are the results of the magnetic springs, which originate from the existence of four sets of repulsive magnets.

In this work, we use the following model of forces generated by magnetic springs

$$F_{si}(x_i) = k_{i1}x_i + k_{i3}x_i^3 + k_{i5}x_i^5; \quad i = 1, 2. \quad (3)$$

In previous works [48, 49] we used a more complicated model of forces generated by magnetic springs

$$F_{si}(x_i) = F_{\text{MOi}} \left[\frac{1}{\{1 + d_i(\delta_i - x_i)\}^4} - \frac{1}{\{1 + d_i(\delta_i + x_i)\}^4} \right]; \quad i = 1, 2, \quad (4)$$

where F_{MOi} , d_i and δ_i are some parameters. In Sec. 2.4 it is shown that the model (3) can replace the model (4).

2.3 Non-dimensional equations of motion

Let us introduce dimensionless time $\tau = \omega_n t$, where ω_n is the frequency of small vibrations of the first body of mass m_1 , with the second body immobilized, for average stiffness:

$$\omega_n = \sqrt{\frac{\frac{k_\xi + k_\eta}{2} + k_{11}}{m_1}}. \quad (5)$$

The subsequent connections can be established between the derivatives of actual and dimensionless time:

$$\frac{d(\dots)}{dt} = \frac{d(\dots)}{d\tau} \frac{d\tau}{dt} = \omega_n \frac{d(\dots)}{d\tau}.$$

Furthermore, we establish the non-dimensional displacements of the system as $u_i = \frac{x_i}{\delta_1}$; $i = 1, 2$. Thus, we may express the following relations: $\dot{x}_i = \omega_n \delta_1 u'_i$, $\ddot{x}_i = \omega_n^2 \delta_1 u''_i$; $i = 1, 2$, and $\Omega = \omega_n \omega$, where it is used the notation $(\dots)' = \frac{d(\dots)}{d\tau}$ and $\omega = \varphi'$ denotes the non-dimensional angular frequency of parametric forcing.

By applying the previously defined relationships, the original governing equation of motion (1) can be transformed into its dimensionless form:

$$u''_1 + 2\zeta_1 u'_1 + \sigma_1 f_0(u'_1) + (p + q \cos(2\omega\tau))(u_1 - u_2) + (1 - p)u_1 + \kappa_{13}u_1^3 + \kappa_{15}u_1^5 = 0, \quad (6a)$$

$$u''_2 + 2\zeta_2 u'_2 + \sigma_2 f_0(u'_2) + \mu(p + q \cos(2\omega\tau))(u_2 - u_1) + \kappa_{21}u_2 + \kappa_{23}u_2^3 + \kappa_{25}u_2^5 = 0, \quad (6b)$$

where we defined and implemented the subsequent parameters (note that $p + \kappa_{11} = 1$):

$$\zeta_i = \frac{c_i}{2m_i\omega_n}, \quad \sigma_i = \frac{T_i}{m_i\omega_n^2\delta_1}, \quad p = \frac{k_\xi + k_\eta}{2m_1\omega_n^2}, \quad q = \frac{k_\xi - k_\eta}{2m_1\omega_n^2}, \quad \kappa_{ij} = \frac{\delta_1^{j-1}}{m_i\omega_n^2} k_{ij}, \quad \mu = \frac{m_1}{m_2}. \quad (7)$$

During numerical simulations using dimensionless equations (6), the non-smooth dry friction terms $f_0(u'_i)$ are replaced by their smooth counterparts $f_{0r}(\alpha u'_i)$ ($i = 1, 2$), where the corresponding smooth function is defined as

$$f_{0r}(v) = \frac{v}{\sqrt{v^2 + 1}}, \quad (8)$$

and where it is assumed $\alpha = 10^3$.

2.4 The system parameters

The parameters of the investigated dynamical system for the exemplary analyses performed in this work are based on the parameters measured and identified on the real experimental stand of the same dynamical system but having 1DOF, i.e., with a fixed cart of mass m_2 [48, 49]. Additionally, it is assumed that the motion resistances in the linear rolling bearings and the magnetic springs are the same along both carts with masses m_1 and m_2 .

Based on exemplary parameters of magnetic spring identified on a real experimental stand: $F_{M01} = 400.96$ N, $d_1 = 46.628$ m $^{-4}$, $\delta_1 = 0.02$ m, it can be proved that model

(3) is sufficient to replace model (4) (see Fig. 2), where two versions of the approximation of the original model (4) are shown: using a 3rd degree polynomial (2a) and a 5th degree polynomial (2b), i.e., using model (3). The fitting was performed by minimizing the mean square of the difference between the corresponding characteristics in the interval $\langle -\delta_1, \delta_1 \rangle$. It was found that the 5th-order polynomial approximation captures the behavior of the original stiffness function with high accuracy over the full range of interest. In contrast, while the 3rd-order polynomial provides a reasonable approximation in terms of average fit, it exhibits significant discrepancies in the slope, particularly near $x_1 = 0$. This deviation alters the extracted linear stiffness coefficient k_{11} and consequently affects all related dimensionless parameters. Although the underlying physical system remains unchanged, such a change in representation introduces inconsistencies in the nondimensional model. Therefore, to maintain consistency in parameter scaling and preserve the fidelity of the model, only the 5th-order polynomial representation is used in the following analysis.

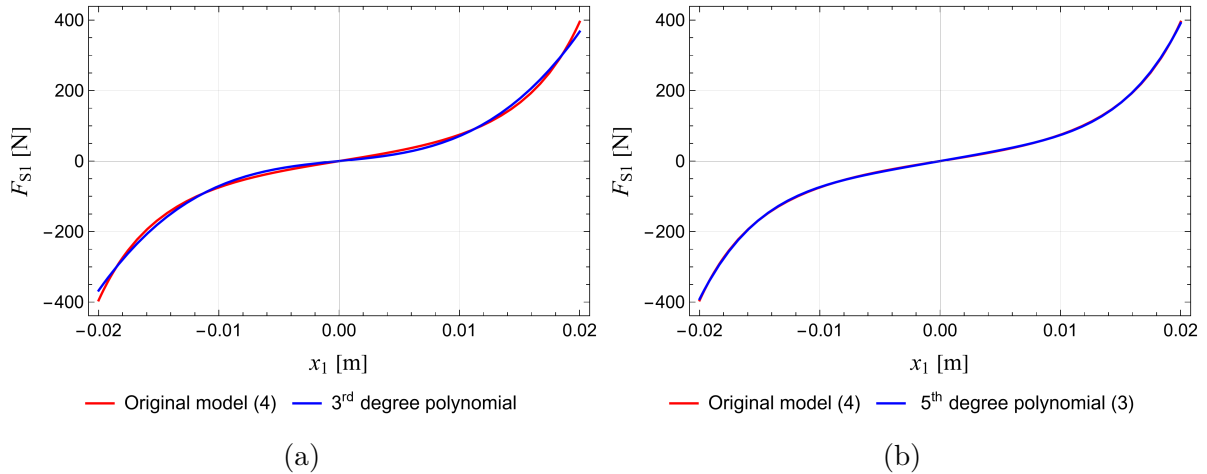


Figure 2: Characteristics of the magnetic force: original model (4) and its approximations by 3rd degree (2a) and 5th (2b) degree polynomial models.

In the remainder of the work, we will investigate two variants of the dynamic system: with different masses $m_1 = 4.55$ kg, $m_2 = 8.72$ kg (A) and with equal masses $m_1 = m_2 = 8.72$ kg (B). The corresponding real parameters of different variants of the system are gathered in Table 1, while the parameters of the corresponding nondimensional system can be found in Table 2. Such a choice of variants of the mass values of both oscillators is justified by the possibility of carrying out an appropriate experiment, because the value of $m_2 = 8.72$ kg corresponds to the actual mass of the second cart on the experimental stand (it contains a stepper motor driving the beam connecting both oscillators). On the other hand, it is possible to add mass to the first trolley and make it equal to the mass of the second trolley. Table 1 also presents the relations for some parameters that link them with other dimensionless parameters of the system, which are valid for the special case under consideration, in which the dimensional parameters of the motion resistances in the bearings and the magnetic springs are the same for both carts.

Table 1: Parameters of dimensional model.

parameter	unit	model version/parameters values	
		A	B
m_1	kg	4.55	8.72
m_2	kg	8.72	8.72
k_ξ	N/m	4336	
k_η	N/m	271	
$\delta_1 = \delta_2$	m	0.02	
$F_{M01} = F_{M02}$	N	401.0	
$d_1 = d_2$	m^{-4}	46.63	
$k_{11} = k_{21}$	N/m	$6.0 \cdot 10^3$	
$k_{13} = k_{23}$	N/m ³	$7.12 \cdot 10^6$	
$k_{15} = k_{25}$	N/m ⁵	$6.70 \cdot 10^{10}$	
$c_1 = c_2$	N · s/m	16.48	
$T_1 = T_2$	N	1.512	

Table 2: Parameters of non-dimensional model.

parameter	model version/parameters values	
	A	B
μ	0.5219	1
p	0.2775	
q	0.2449	
κ_{13}	0.343	
κ_{15}	1.291	
κ_{21}	$\mu(1 - p)$	
κ_{23}	$\mu \kappa_{13}$	
κ_{25}	$\mu \kappa_{15}$	
ζ_1	$0.03062 \mu^{-1/2}$	
ζ_2	$\mu \zeta_1$	
σ_1	0.009106	
σ_2	$\mu \sigma_1$	

3 Analytical solutions

In this section, our objective is to perform an analysis of the system (6) using a perturbation method. We utilize the CxA method as recommended in reference [52]. Therefore, we utilize the methodology above to provide analytical solutions that closely correspond to the numerical solutions.

3.1 Approximate analytical solutions by CxA method

To obtain the amplitudefrequency response, the ComplexificationAveraging (CxA) method [53,54] is utilized, which has proven effective in analyzing strongly nonlinear mechanical systems. This approach involves decomposing the system's motion into fast oscillatory components and slowly varying amplitude modulations through the introduction of complex variables. Subsequently, the amplitude modulation dynamics are averaged over one period of the base excitation frequency. Recent developments have extended this method to support averaging over multiple excitation frequencies [55]. The first step in the CxA procedure is to define the time-dependent complex variables representing the modulated amplitudes, $A_1 \in \mathbb{C}$ and $A_2 \in \mathbb{C}$:

$$2A_1(\tau)e^{i\omega\tau} = u_1(\tau) - i\frac{u'_1(\tau)}{\omega}, \quad 2A_2(\tau)e^{i\omega\tau} = u_2(\tau) - i\frac{u'_2(\tau)}{\omega}, \quad (9)$$

where $i = \sqrt{-1}$ is the complex number. The variables u_1 , u_2 , and the derivatives of these variables as functions of A_1 and A_2 are derived by adding and subtracting Eq. (9) and their complex conjugates:

$$u_1 = A_1e^{i\omega\tau} + \bar{A}_1e^{-i\omega\tau}, \quad u_2 = A_2e^{i\omega\tau} + \bar{A}_2e^{-i\omega\tau}, \quad (10a)$$

$$u'_1 = i\omega(A_1e^{i\omega\tau} - \bar{A}_1e^{-i\omega\tau}), \quad u'_2 = i\omega(A_2e^{i\omega\tau} - \bar{A}_2e^{-i\omega\tau}), \quad (10b)$$

where \bar{A} denotes the conjugate of a complex-valued function A . Taking the time derivative of Eq. (9) to get the acceleration in terms of new variables A_1 and A_2 below:

$$2A'_1e^{i\omega\tau} + 2i\omega A_1e^{i\omega\tau} = u'_1 - i\frac{u''_1}{\omega}, \quad 2A'_2e^{i\omega\tau} + 2i\omega A_2e^{i\omega\tau} = u'_2 - i\frac{u''_2}{\omega}. \quad (11)$$

Using Eq. (10b) into Eq. (11), which yields

$$u''_1 = 2i\omega A'_1e^{i\omega\tau} - \omega^2 u_1, \quad u''_2 = 2i\omega A'_2e^{i\omega\tau} - \omega^2 u_2. \quad (12)$$

Using Eqs. (10), & (12) in Eq. (6), multiplying by $e^{-i\omega\tau}$ and then averaging with the forcing frequency ω results in

$$2\zeta_1\omega A_1 + 2i\omega A'_1 + A_1 - pA_2 + \frac{q}{2}(\bar{A}_1 - \bar{A}_2) + 3\kappa_{13}A_1^2\bar{A}_1 + 10\kappa_{15}A_1^3\bar{A}_1^2 - \omega^2 A_1 + \sigma_1 f_0(i\omega A_1e^{i\omega\tau} - i\omega \bar{A}_1e^{-i\omega\tau}) = 0, \quad (13a)$$

$$2i\zeta_2\omega A_2 + 2i\omega A'_2 + \kappa_{21}A_2 - \mu p A_1 + \mu p A_2 + \frac{\mu q}{2}(\bar{A}_2 - \bar{A}_1) + 3\kappa_{23}A_2^2\bar{A}_2 + 10\kappa_{25}A_2^3\bar{A}_2^2 - \omega^2 A_2 + \sigma_2 f_0(i\omega A_2e^{i\omega\tau} - i\omega \bar{A}_2e^{-i\omega\tau}) = 0. \quad (13b)$$

We can expand the dry friction function in a Fourier series to capture all the resonant aspects of the following form

$$f_0(u'_1) = f_0(i\omega A_1e^{i\omega\tau} - i\omega \bar{A}_1e^{-i\omega\tau}) = \sum_{-\infty}^{+\infty} r_m e^{im\omega\tau}, \quad (14)$$

and

$$f_0(u'_2) = f_0(i\omega A_2e^{i\omega\tau} - i\omega \bar{A}_2e^{-i\omega\tau}) = \sum_{-\infty}^{+\infty} s_n e^{in\omega\tau}. \quad (15)$$

The Fourier coefficients r_m and s_n in Eqs. (14) and (15) respectively, can be expressed as follows:

$$r_m = \frac{1}{2\pi} \int_0^{2\pi} f_0(i\omega A_1 e^{i\omega\tau} - i\omega \bar{A}_1 e^{-i\omega\tau}) e^{im\omega\tau} d\tau, \quad (16)$$

and

$$s_n = \frac{1}{2\pi} \int_0^{2\pi} f_0(i\omega A_2 e^{i\omega\tau} - i\omega \bar{A}_2 e^{-i\omega\tau}) e^{in\omega\tau} d\tau. \quad (17)$$

In the Fourier series (16) and (17), the terms $r_1 e^{i\omega\tau}$ and, $s_1 e^{i\omega\tau}$ respectively, are only the resonant terms. To eliminate secular terms, the resonant terms in Eq. (13) must be removed. This yields:

$$\begin{aligned} 2\zeta_1 \omega A_1 + 2i\omega A'_1 + A_1 - pA_2 + \frac{q}{2}(\bar{A}_1 - \bar{A}_2) + 3\kappa_{13} A_1^2 \bar{A}_1 \\ + 10\kappa_{15} A_1^3 \bar{A}_1^2 - \omega^2 A_1 + \sigma_1 r_1 = 0, \end{aligned} \quad (18a)$$

$$\begin{aligned} 2i\zeta_2 \omega A_2 + 2i\omega A'_2 + \kappa_{21} A_2 - \mu p A_1 + \mu p A_2 + \frac{\mu q}{2}(\bar{A}_2 - \bar{A}_1) + 3\kappa_{23} A_2^2 \bar{A}_2 \\ + 10\kappa_{25} A_2^3 \bar{A}_2^2 - \omega^2 A_2 + \sigma_2 s_1 = 0. \end{aligned} \quad (18b)$$

Introducing the following polar forms below:

$$A_1 = \frac{1}{2} a_1 e^{i\alpha_1}, \quad A_2 = \frac{1}{2} a_2 e^{i\alpha_2}, \quad (19)$$

for separating the real and imaginary parts. Eq. (19) gives us $A'_1 = \frac{1}{2}(a'_1 + ia_1 \alpha'_1) e^{i\alpha_1}$ and $A'_2 = \frac{1}{2}(a'_2 + ia_2 \alpha'_2) e^{i\alpha_2}$, where ' shows the time derivative. A new form $u_1 = a_1 \cos \psi_1$ and $u_2 = a_2 \cos \psi_2$ are derived by incorporating an additional parameter, specifically $\psi_1 = \omega\tau + \alpha_1$ and $\psi_2 = \omega\tau + \alpha_2$ respectively. In this context, the term "dry friction" is expressed as follows for the scenario $a_1, a_2 > 0$, The dry friction term is expressed as follows:

$$r_1 = \frac{1}{2\pi} \int_0^{2\pi} f_0(-a_1 \sin \psi_1) e^{-i\psi_1} e^{i\alpha_1} d\psi_1, \quad \Rightarrow \quad \frac{2i}{\pi} e^{i\alpha_1}, \quad (20)$$

and

$$s_1 = \frac{1}{2\pi} \int_0^{2\pi} f_0(-a_2 \sin \psi_2) e^{-i\psi_2} e^{i\alpha_2} d\psi_2, \quad \Rightarrow \quad \frac{2i}{\pi} e^{i\alpha_2}. \quad (21)$$

For the steady-state case, the time derivative of A_1 & A_2 will be equal to zero. So substituting the $A'_1 = A'_2 = 0$ into Eq. (13) for the steady case, and then using the Eqs. (19), (20), and (21) into Eq. (13). Then, after a long but smooth calculation, we will get the following form of equations:

$$\begin{aligned} \frac{5}{8} \kappa_{15} a_1^5 + \frac{3}{4} \kappa_{13} a_1^3 - p a_2 e^{i(\alpha_2 - \alpha_1)} - \frac{q}{2} a_2 e^{-i(\alpha_2 + \alpha_1)} + \frac{q}{2} a_1 e^{-2i\alpha_1} \\ + 2i\zeta_1 \omega a_1 - \omega^2 a_1 + a_1 + \frac{4i\sigma_1}{\pi} = 0, \end{aligned} \quad (22a)$$

$$\begin{aligned} \frac{5}{8} \kappa_{25} a_2^5 + \frac{3}{4} \kappa_{23} a_2^3 - \mu p a_1 e^{i(\alpha_1 - \alpha_2)} - \frac{q}{2} \mu a_1 e^{-i(\alpha_1 + \alpha_2)} + \frac{q}{2} \mu a_2 e^{-2i\alpha_2} \\ + 2i\zeta_2 \omega a_2 - \omega^2 a_2 + \mu p a_2 + \kappa_{21} a_2 + \frac{4i\sigma_2}{\pi} = 0. \end{aligned} \quad (22b)$$

Separating the real and imaginary parts of Eqs. (22a) & (22b), which gives us the following system of equations:

$$\begin{aligned} \frac{q}{2}a_1 \cos(2\alpha_1) - \frac{q}{2}a_2 \cos(\alpha_2 + \alpha_1) + \frac{3}{4}\kappa_{13}a_1^3 + \frac{5}{8}\kappa_{15}a_1^5 \\ + (1 - \omega^2)a_1 - pa_2 \cos(\alpha_2 - \alpha_1) = 0, \end{aligned} \quad (23a)$$

$$2\omega\zeta_1a_1 - pa_2 \sin(\alpha_2 - \alpha_1) - \frac{q}{2}a_1 \sin(2\alpha_1) + \frac{q}{2}a_2 \sin(\alpha_2 + \alpha_1) + \frac{4}{\pi}\sigma_1 = 0, \quad (23b)$$

$$\begin{aligned} \frac{q}{2}\mu a_2 \cos(2\alpha_2) - \frac{q}{2}\mu a_1 \cos(\alpha_1 + \alpha_2) + \frac{3}{4}\kappa_{23}a_2^3 + \frac{5}{8}\kappa_{25}a_2^5 \\ + (\kappa_{21} + \mu p - \omega^2)a_2 - \mu p a_1 \cos(\alpha_1 - \alpha_2) = 0, \end{aligned} \quad (23c)$$

$$2\omega\zeta_2a_2 - \mu p a_1 \sin(\alpha_1 - \alpha_2) - \frac{q}{2}\mu a_2 \sin(2\alpha_2) + \frac{q}{2}\mu a_1 \sin(\alpha_1 + \alpha_2) + \frac{4}{\pi}\sigma_2 = 0. \quad (23d)$$

Note that Eqs. (23a) & (23b) are the real and imaginary parts of Eq. (22a) and Eqs. (23c) & (23d) are the real and imaginary parts of Eq. (22b) respectively. The stability of the solutions of Eqs. (23) is judged from the Jacobian of Eqs. (18).

4 Dynamical Analysis

In this section, we analyzed the considered system analytically and numerically and also performed a comparison analysis of analytical and numerical solutions. We have divided this section into two parts. Subsection (4.1) describes the analysis for different masses $m_1 \neq m_2$, and Subsection (4.2) describes the behavior of the considered system for the same masses $m_1 = m_2$.

4.1 Bifurcation analysis for different masses ($m_1 \neq m_2$)

This subsection explains the results of the bifurcation analysis obtained analytically and numerically for a 2DOF parametric oscillators with different masses.

For the case of unequal masses, the parameter set A is held in Table 2. A continuation technique [56] is used to solve Eqs. (23a-23d) numerically. The results are plotted in Figs. 3 in the case of friction and no friction ($\sigma_1 = 0$). The solid curves represent the stable solutions, while the dashed curves indicate unstable solutions, and the stability is computed from the Jacobian of Eqs. (23a-23d). The amplitude curve of the first mass a_1 is similar to the 1DOF case investigated in [49]. The second mass shows a fold where the amplitude saturates just below $a_2 = 0.1$. To compare the validity, the EOMs Eqs. (6a-6b) are simulations with a Runge-Kutta scheme in Figs. 4 and Figs. 5 for the cases without and with friction. The excitation ω in the RK-scheme is increased stepwise from 0.8 to 1.8. The RMS of the displacement multiplied by $\sqrt{2}$ after steady-state is recorded at each frequency step. It can be seen that the full EOMs closely follow the analytical curve, especially near $\omega = 1$. For ω near the jump, there is a slight deviation.

Fig. 6 displays bifurcation diagrams obtained by using a Poincaré map that shows the dynamic behavior of a parametrically excited two-degree-of-freedom (2-DOF) system exhibiting fifth-degree stiffness nonlinearity. The previous three Figs. 3, 4, and 5 be also seen as bifurcation diagrams obtained from other methods, and we have compared them in Fig. 6. The excitation frequency ω is utilized as the control parameter to examine forward and backward sweeps, with outcomes presented for three observables.

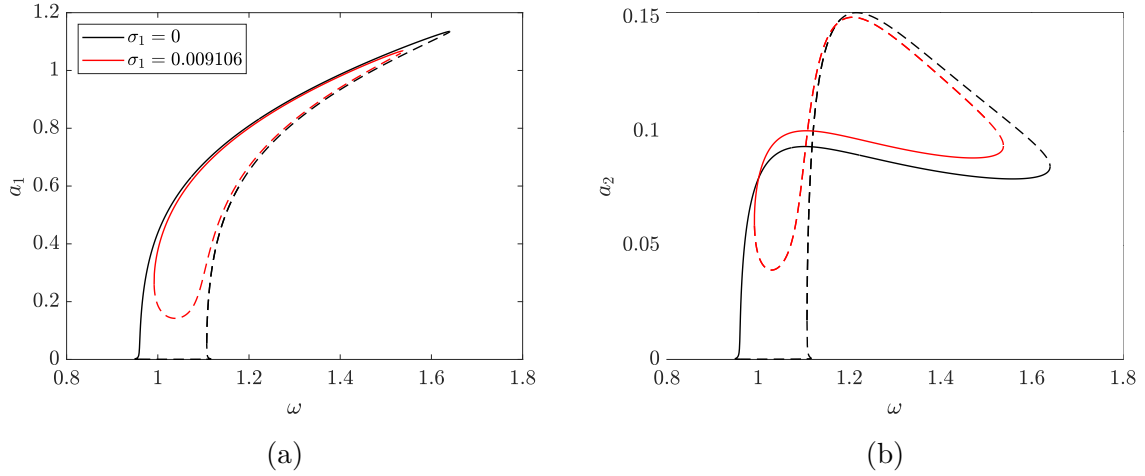


Figure 3: Comparing the analytical results from CxA for the first mass (a) and the second mass (b) in the case of $m_1 \neq m_2$.

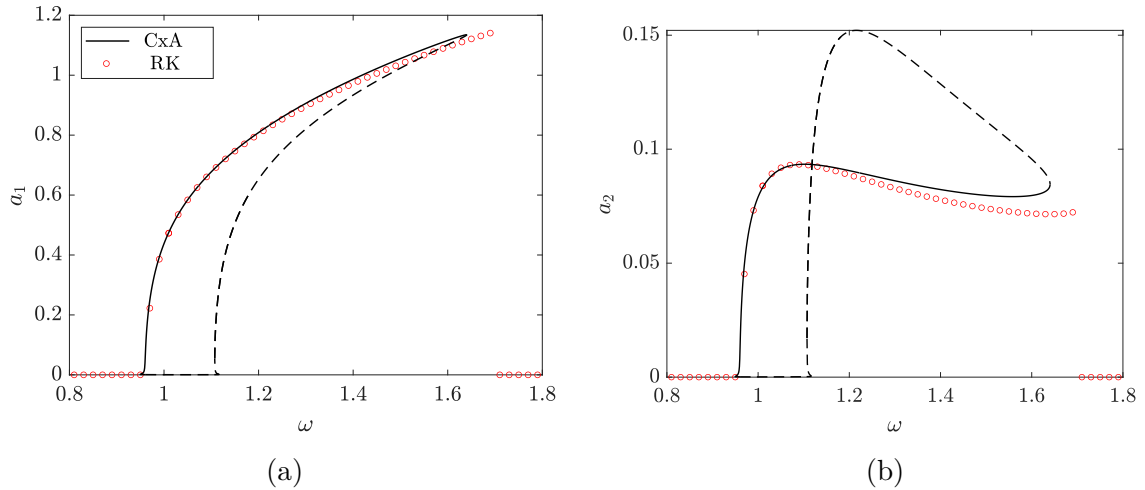


Figure 4: Comparing the analytical results with a Runge-Kutta sweep simulation for the first mass (a) and the second mass (b) where $\sigma_1 = 0$ and $m_1 \neq m_2$.

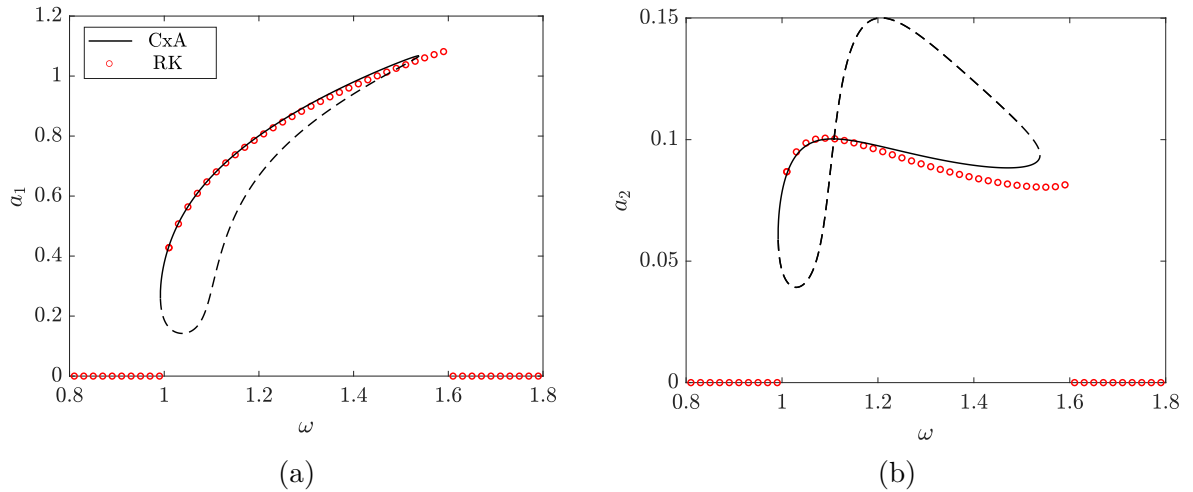


Figure 5: Comparing the analytical results with a Runge-Kutta sweep simulation for the first mass (a) and the second mass (b) where $\sigma_1 = 0.009106$ and $m_1 \neq m_2$.

We have compared the approximate analytical results obtained by the CxA method with the numerical results in Figs. 6a and 6c, where we observed a good agreement between analytical and numerical results.

Figs. 6a and 6b illustrate the bifurcation diagrams of the local maxima for the primary and secondary coordinates, u_1 and u_2 , respectively, along with the bifurcation diagram of the largest Lyapunov exponent λ_1 6d with the bifurcation parameter ω . Lyapunov exponents are used to quantify a systems sensitivity to initial conditions. They help distinguish between periodic, quasi-periodic, and chaotic behavior. This makes them essential for analyzing the long-term stability of nonlinear systems. The maxima were derived from the solutions by Poincaré sampling at each excitation period, with maxima identified when the corresponding velocities intersect zero with a negative slope. Fig. 6c presents an auxiliary diagram for u_2 , obtained when the velocity of the second oscillator is zero.

The numerical continuation was executed utilizing both forward (blue) and backward (red) frequency sweeps. During the forward sweep, ω was adjusted from 1.15 to 1.70, whereas in the backward sweep, it ranged from 1.15 to 0.90. The initial conditions were established as $u_1 = 0.55$, $u'_1 = 0.55$, $u_2 = 1.1$, and $u'_2 = -1.1$.

The bifurcation diagrams indicate a stable trivial solution for low values of ω , succeeded by the onset of large-amplitude periodic oscillations with increasing frequency. The pronounced reliance on the frequency sweep direction underscores the multistable characteristics of the system's response. The seamless forward advancement contrasts with the delayed bifurcation during the backward sweep, indicating the existence of fold bifurcations and the potential separation of basins of attraction.

Fig. 7 illustrates the steady-state dynamics of the 2DOF system under parametric excitation at a driving frequency of $\omega = 1.15$, with initial conditions are $u_1 = 0.55$, $u'_1 = 0.22$, $u_2 = 1.1$, and $u'_2 = -1.1$. Following the elimination of transients exceeding 100 excitation cycles, the system dynamics were examined during the next 50 periods. Figs. 7a and 7b illustrate the time-domain responses of u_1 and u_2 , respectively, demonstrating continuous periodic oscillations characterized by varying amplitudes and frequency components. The steady-state trajectories indicate that both oscillators are synchronized to the external excitation frequency, albeit with amplitude and phase discrepancies due to modal coupling and stiffness asymmetry. The associated phase portraits are illustrated in Figs. 7c and 7d for the (u_1, \dot{u}_1) and (u_2, \dot{u}_2) planes, respectively. Both trajectories create closed loops, validating the regularity noted in the temporal histories and also illustrating the associated Poincaré maps, sampled with velocity components \dot{u}_1 and \dot{u}_2 intersecting zero in the negative direction. The maps in Figs. 7c and 7d, represented in (u_1, \dot{u}_1) and (u_2, \dot{u}_2) coordinates, exhibit distinct singular points, signifying a phase-locked periodic orbit. Fig. 7e further depicts the projection in the (u_2, u_1) plane, demonstrating a robust correlation while maintaining a non-identical coupling between the two coordinates. The periodic nature of the solution is validated by a positive greatest Lyapunov exponent λ_1 , with the method of computation illustrated in Fig. 8, and the total number of periods of external forcing is denoted by n (on the x-axis).

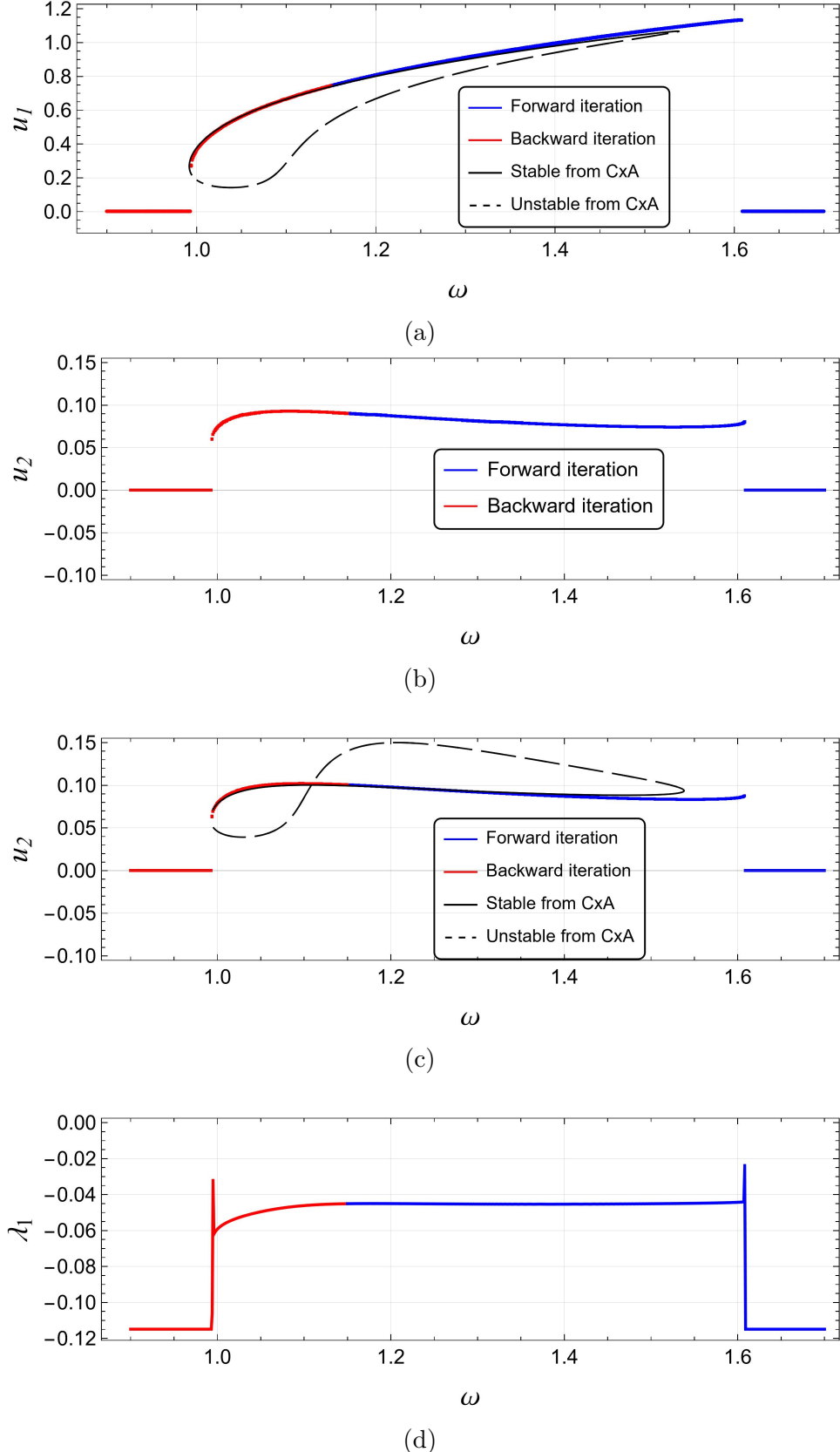


Figure 6: Illustrating the bifurcation plot of the local maxima of u_1 for coordinates u_1 (a) and u_2 (b), the local maxima of $u_2(\tau)$ (c), and the largest Lyapunov exponent λ_1 (d) as the excitation frequency ω ranges from 1.15 to 0.90 (for backward) and 1.15 to 1.70 (for forward) and analytical results obtained from the CxA method: A comparison analysis.

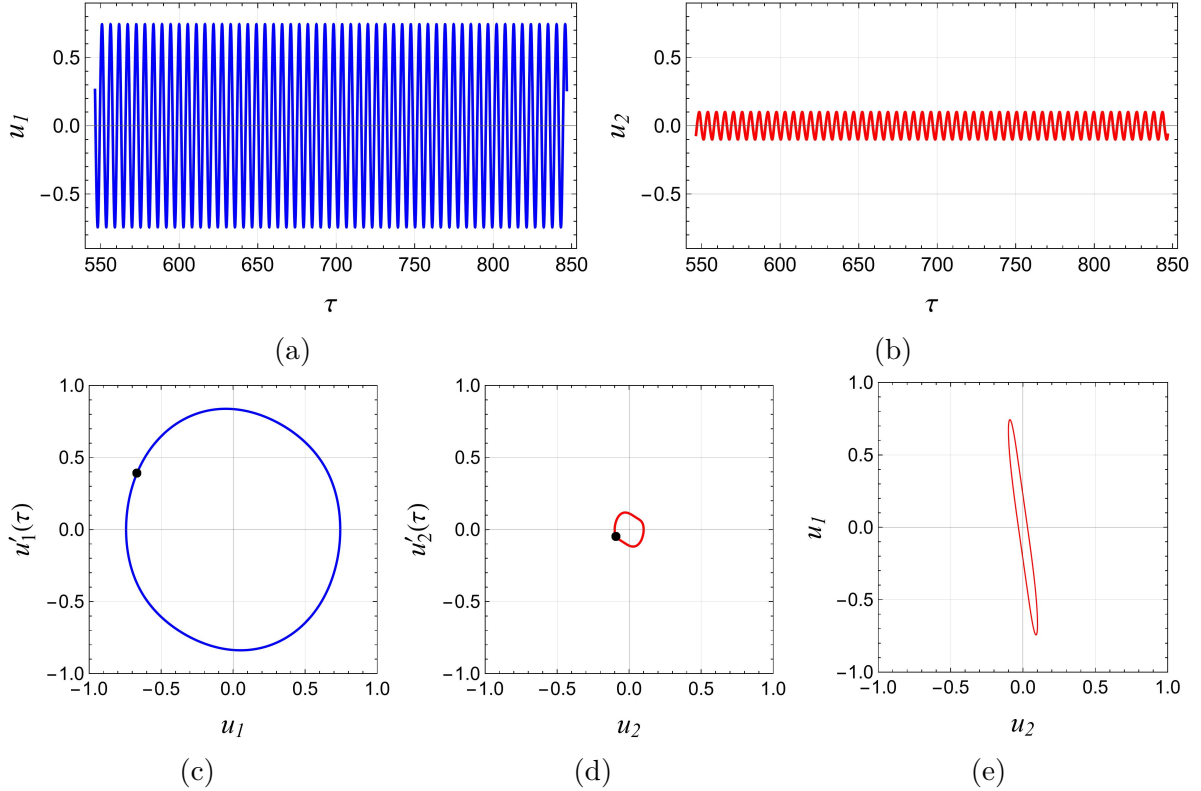


Figure 7: The time-domain plots (ab) show steady-state oscillations for u_1 and u_2 after an initial transient phase of 100 periods, $\omega = 1.15$, The phase-space plots and single points in Poincaré maps (c) and (d) display closed-loop trajectories, indicating periodic, stable motion in antiphase mode.

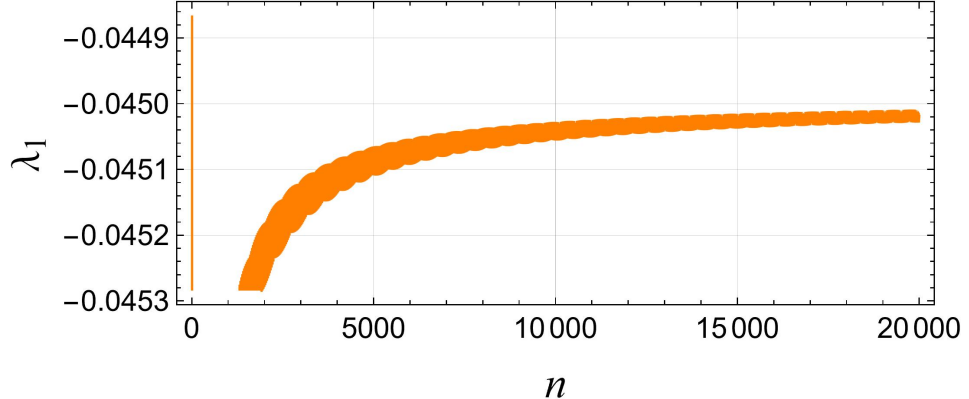


Figure 8: The maximal Lyapunov exponent λ_1 as a function of the number of external forcing periods n for $\omega = 1.15$.

4.2 Bifurcation analysis for same masses ($m_1 = m_2$)

This subsection explains the results of the bifurcation analysis obtained analytically and numerically for a 2DOF parametric oscillators with the same masses.

For the case of equal masses, the parameter set B holds in Table 2. The analytical results are plotted in Figs. 9 in the case of friction and no friction ($\sigma_1 = 0$). Figs. 9a and 9b show the same frequency response as the system is now symmetrical. Only the case

without friction is shown in these figures, as they are close to the curves with friction. Compared to the case of unequal mass, there are solutions over a much wider frequency range; however, most of the branches are unstable except closer to $\omega = 1$. When zoomed in, in Figs. 9c and 9d, it can be seen that $\omega = 1.08$, the stable branch has a pitchfork bifurcation before becoming unstable. For the case with friction, the pitchfork shifts to the right. On the two stable branches of the pitchfork, the response becomes unstable starting from $\omega = 1.1$. Observing the eigenvalues of the Jacobian, a Hopf bifurcation is observed where complex eigenvalues go from negative to positive real values. This hints at a quasi-periodic response in the time domain, where the amplitude will modulate.

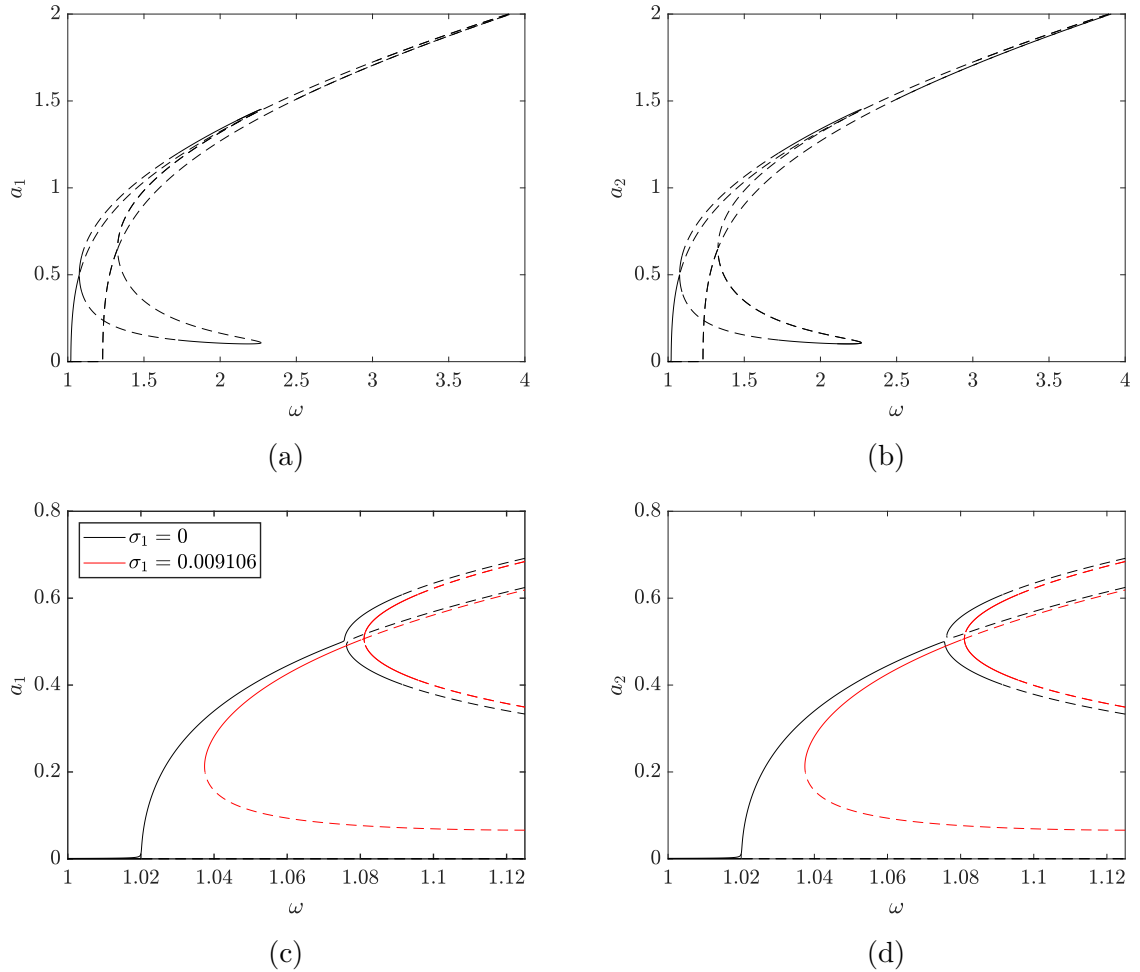


Figure 9: Comparison of the analytical results (23) from the CxA method with and without dry friction: (a,b) represents the results without dry friction, and (c,d) represents the behavior of the system with dry friction for $\sigma_1 = 0.009106$ and without dry friction for $\sigma_1 = 0$, and $m_1 = m_2$.

The RMS of the RK simulation is plotted in Figs. 10 without friction and Fig. 11 with friction. For no friction, it can be seen that after the pitchfork bifurcation, the first mass tends to the upper branch Fig. 10a while the other mass tends to the lower branch. The same can be seen in the case of friction. Once both the upper and lower branches become unstable, the RMS does not follow a trend dictated by the branches. A chaotic response appears, which will be studied later. Fig. 12 displays bifurcation diagrams computed for ω as a control parameter. Diagrams depict the intricate nonlinear

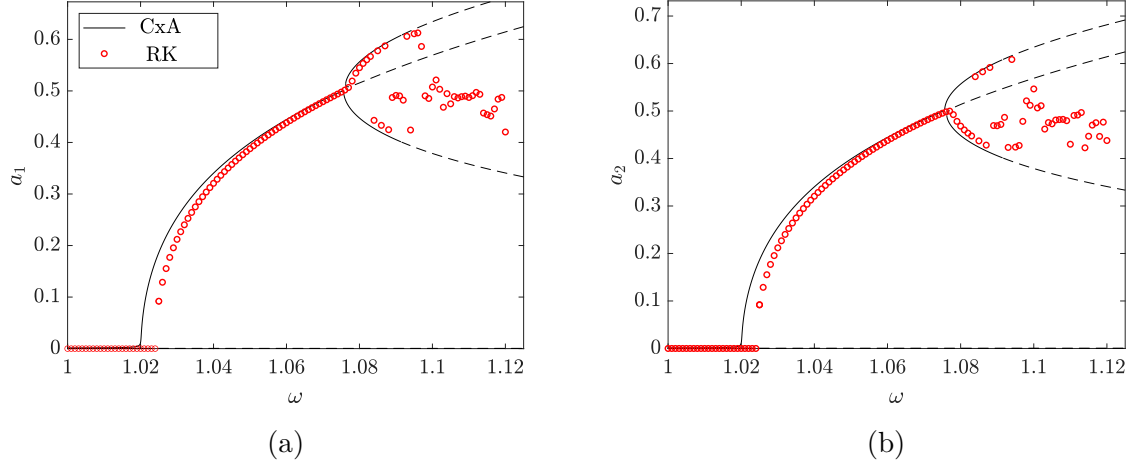


Figure 10: Comparison analysis of analytical results from CxA with the RMS of the RK simulation for m_1 (a) and for m_2 (b) without dry friction $\sigma_1 = \sigma_2 = 0$, in the case of the same masses, $m_1 = m_2$.

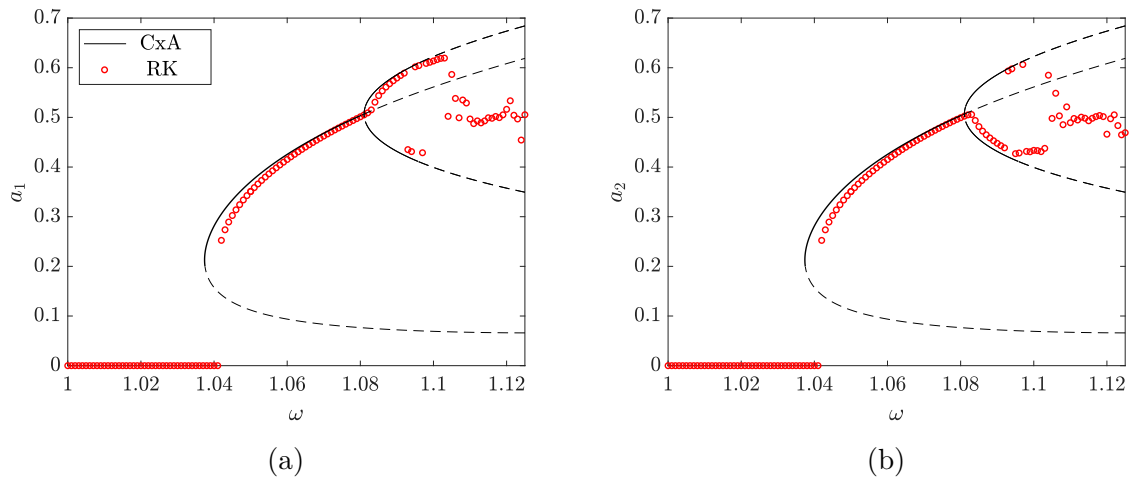


Figure 11: Comparison analysis of analytical results from CxA with the RMS of the RK simulation for m_1 (a) and for m_2 (b) with dry friction $\sigma_1 = 0.009106$, and $\sigma_2 = \mu\sigma_1$, in the case of the same masses, $m_1 = m_2$.

response of a parametrically excited 2DOF system featuring stiffness nonlinearity. The diagrams in Figs. 12a and 12b are created using Poincaré sections obtained at the local maxima of the primary coordinate u_1 , identified when the velocity \dot{u}_1 passes zero with a negative slope, and the bifurcation diagram of the largest Lyapunov exponent λ_1 12d with the bifurcation parameter ω . Moreover, the diagram in Fig. 12c was computed at the local maxima of u_2 , while its velocity was zero ($u'_2 = 0$). The system's reaction is analyzed by both forward (blue) and backward (red) frequency sweeps throughout the range $\omega \in [1.0, 1.15]$, demonstrating the system's sensitivity to initial conditions. The initial conditions are $u_1 = 0.99$, $u'_1 = 0.88$, $u_2 = 1.1$, $u'_2 = 0$, and, emphasizing its multistable characteristics. In the low-frequency range of the control parameter, the system demonstrates a stable trivial solution; however, once it ω surpasses around 1.04, a branch of periodic oscillations arises. Close to $\omega \approx 1.09$, an abrupt change transpires, resulting in complex dynamics characterized by the presence of dense windows in the bifurcation diagrams. This regime signifies the emergence of quasi-periodicity and chaos.

Rich bifurcation dynamics are observed, encompassing periodic, quasiperiodic, and chaotic behaviors. Moreover, the bifurcation diagrams obtained from the Poincaré map align closely with the behavior indicated by the largest Lyapunov exponent. In particular, a positive exponent corresponds to chaotic motion, a zero value reflects quasiperiodic dynamics, and a negative exponent indicates the presence of stable periodic orbits.

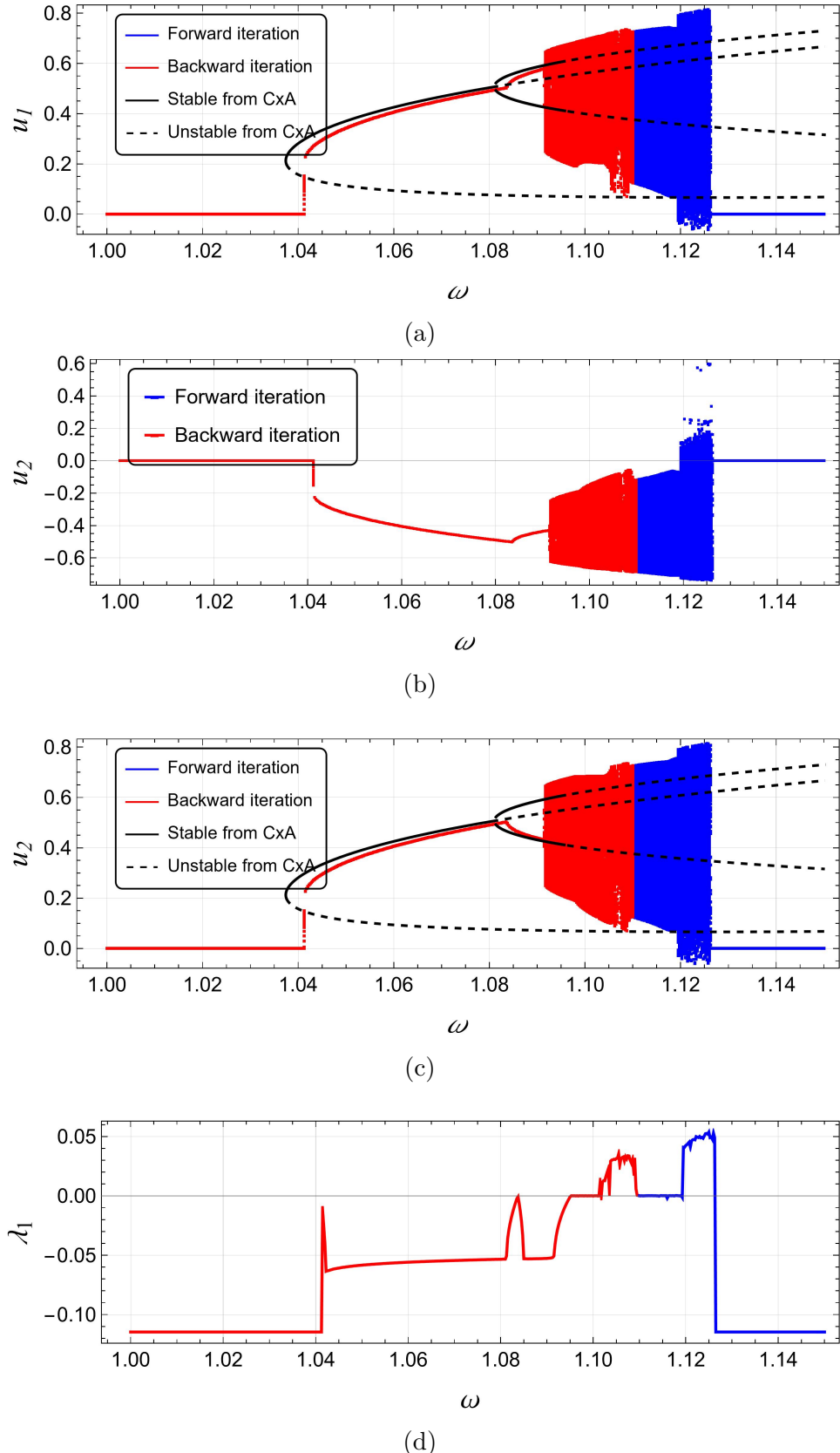


Figure 12: Illustrating the bifurcation plot of the local maxima of u_1 for coordinates u_1 (a) and u_2 (b), the local maxima of $u_2(\tau)$ (c), and the largest Lyapunov exponent λ_1 (d) as the excitation frequency ω ranges from 1.11 to 1.0 (for backward) and 1.11 to 1.15 (for forward) and analytical results obtained from the CxA method: A comparison analysis.

Based on bifurcation diagrams from Fig. 12, selected cases of system motion were analyzed using time series, phase plots, and Poincaré maps.

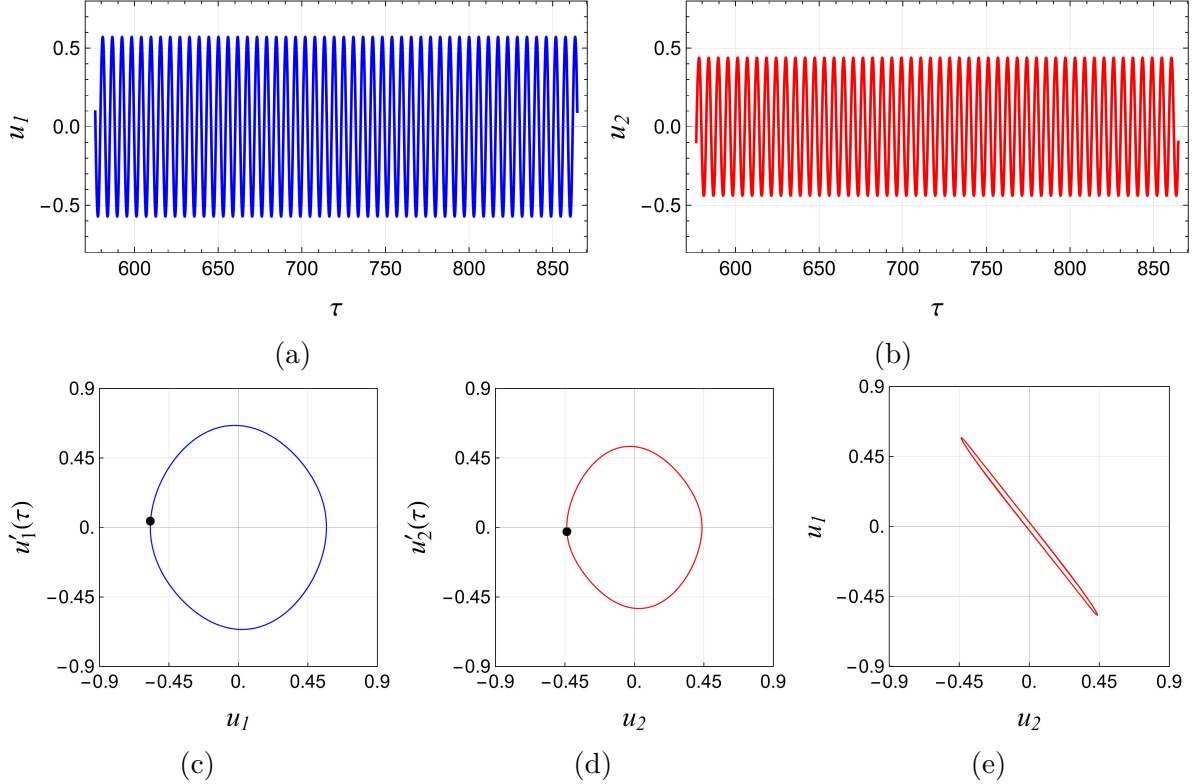


Figure 13: The time-domain plots (ab) show steady-state oscillations for u_1 and u_2 after an initial transient phase of 100 periods, $\omega = 1.09$. The phase-space plots with Poincaré maps (c-d) display closed-loop trajectories, indicating periodic, stable motion in antiphase mode (e). Single Poincaré points also state for regular oscillations.

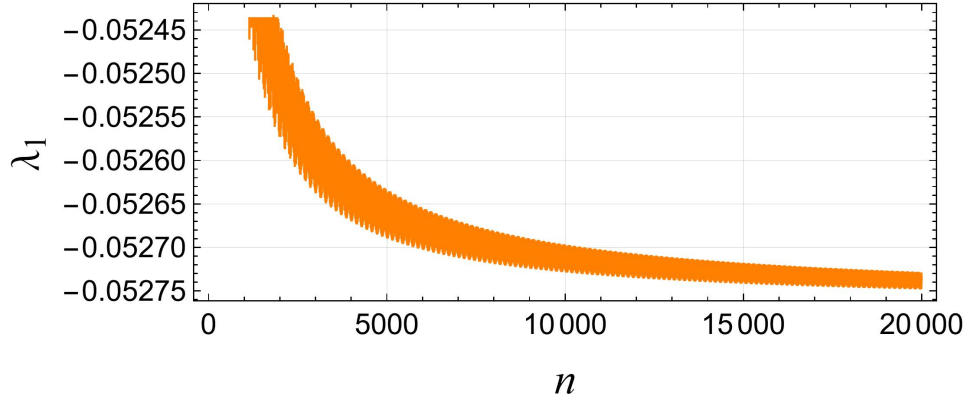


Figure 14: The maximal Lyapunov exponent λ_1 as a function of the number of external forcing periods n for $\omega = 1.09$

Time series displayed in Figs. 13a and 13b were calculated for a driving frequency $\omega = 1.09$ for the initial conditions are $u_1 = 0.20$, $u'_1 = 0.98$, $u_2 = 0.56$, and $u'_2 = 0.045$, and the system experiences periodic oscillations. The phase plots in Figs. 13c and 13d show closed orbits typical for periodic motion. Furthermore, from Fig. 13e, it can be seen that the oscillations are close to the antiphase mode due to the negative slope of the $u_1 - u_2$

curve. The Poincaré maps are presented as black dots in Figs. 13c and 13d. Maps in Fig. 13c were obtained when u_2 archives its local maximum, while those in Fig. 13d were obtained when u_1 archives its local maximum (corresponding to Fig. 12b). Single points observed in all Poincaré maps indicate regular motion in the system. The periodic behavior of the outcome is validated by a positive greatest Lyapunov exponent λ_1 for $\omega = 1.09$, and taking the values of the parameters from Table 2, with the method of computation illustrated in Fig. 14, where n is the total number of periods of external forcing.

A motion is presented in Figs. 15a and 15b show oscillations with fluctuating amplitude and is obtained for frequency $\omega = 1.10$, and the initial conditions are $u_1 = 0.75$, $u'_1 = 0.25$, $u_2 = 0.11$, and $u'_2 = 0.79$. The phase trajectories with Poincaré maps are displayed in Figs. 15c-15d and are composed of many closely spaced and overlapping orbits, which is untypical for periodic motion. The fluctuating amplitude indicates quasi-periodic motion, and it is confirmed by Poincaré maps. Poincaré points form closed curves, confirming the presence of quasi-periodicity resulting from frequency components that are mutually incommensurable, meaning their ratios are irrational and the trajectory never exactly repeats, although it remains bounded and orderly. Oscillations exhibit near antiphase character in Fig. 15e. Fig. 16 presents the quasi-periodic motion, which is validated by a positive greatest Lyapunov exponent λ_1 for the $\omega = 1.10$, as a function of the number of periods of forcing n .

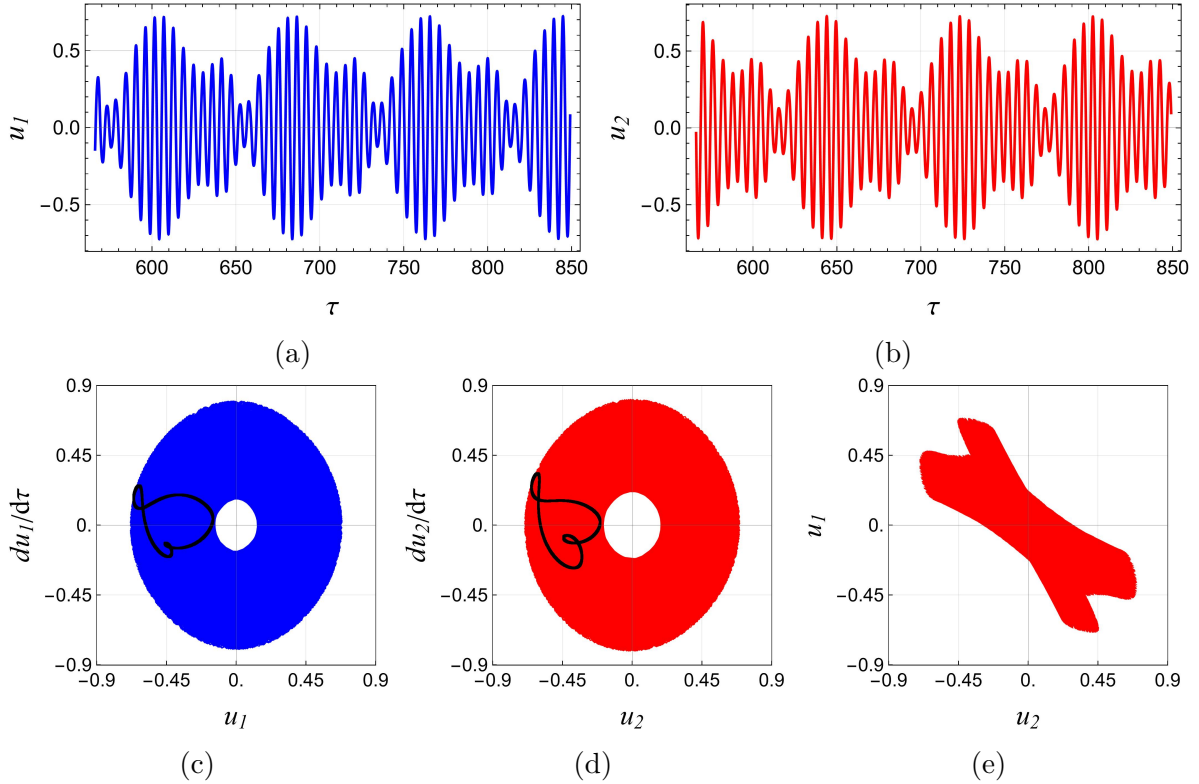


Figure 15: The time-domain plots (top) show near steady-state oscillations for u_1 and u_2 after an initial transient phase of 100 periods, $\omega = 1.10$. The phase-space plots (bottom) display multiple closed-loop trajectories, and the Poincaré section indicates a quasi-periodic motion.

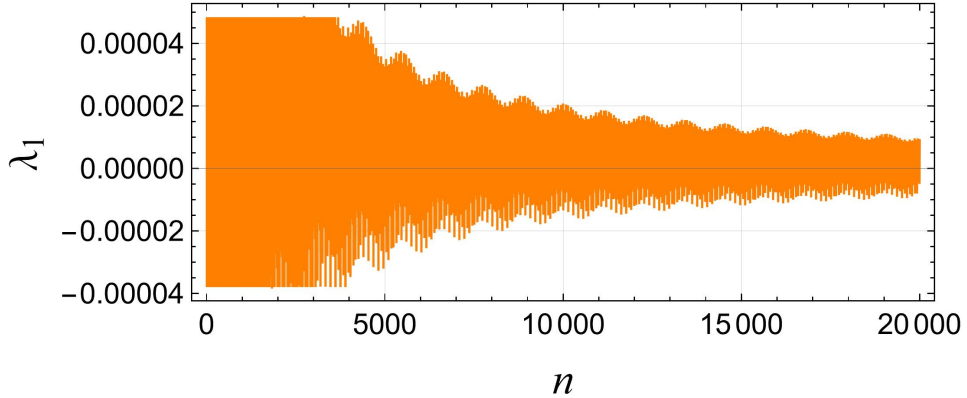


Figure 16: The maximal Lyapunov exponent λ_1 as a function of the number of external forcing periods n for $\omega = 1.10$

In Fig. 17, the time series plots might at first glance suggest the chaotic motion of the oscillators. However, the phase portraits and Poincaré maps clearly indicate that the system operates in a quasi-periodic pattern for the examined frequency $\omega = 1.11$, and the initial conditions are $u_1 = 0.99$, $u'_1 = 0.88$, $u_2 = 1.1$, and $u'_2 = 0$. The quasi-periodic behavior of the results is confirmed by a positive greatest Lyapunov exponent λ_1 for $\omega = 1.11$, as a function of the number of periods of forcing n , and assuming the values of involved parameters from Table 2, with the method of computation presented in Fig. 18.

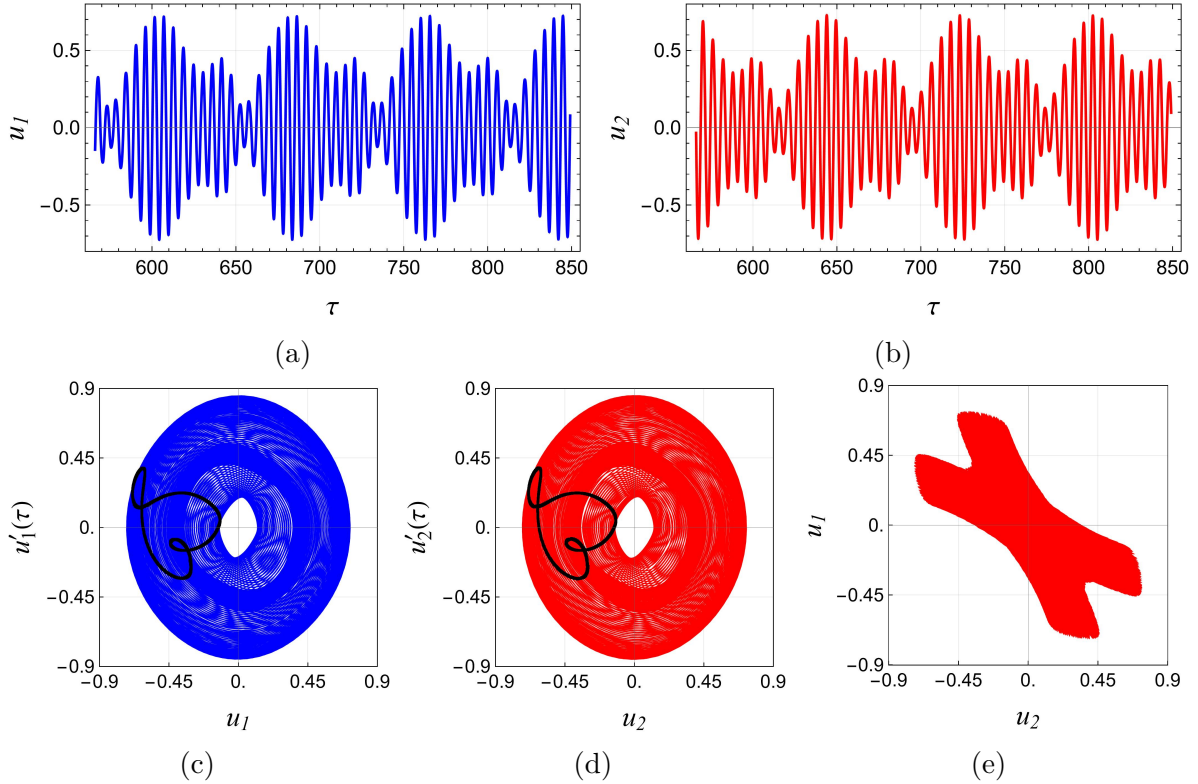


Figure 17: The time-domain plots (top) show near steady-state oscillations for u_1 and u_2 after an initial transient phase of 100 periods, $\omega = 1.11$. The phase-space plots (bottom) display an uncertain trajectory, while the Poincaré maps indicate quasi-periodicity.

It is evident that the studied case represents a further evolution of the quasi-periodic motion analyzed in Fig. 15. The oscillation amplitudes increase with the increase of the

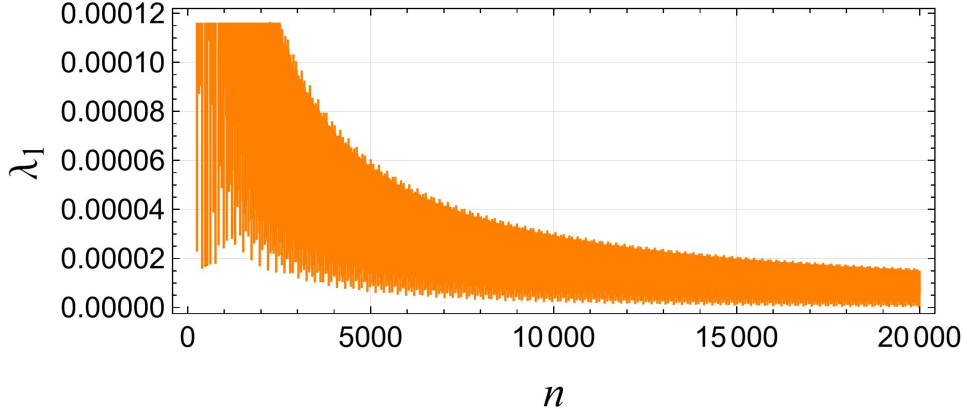


Figure 18: The maximal Lyapunov exponent λ_1 as a function of the number of external forcing periods n for $\omega = 1.11$

control parameter ω , resulting, finally, in non-periodic motion presented in Fig. 19.

The case of system motion considered in Fig. 19 meets the characteristics of a chaotic regime for $\omega = 1.125$ and the initial conditions are $u_1 = 0.99$, $u'_1 = 0.88$, $u_2 = 1.1$, and $u'_2 = 0$. The time series and phase trajectories show a lack of repeatability, and the Poincaré maps form a chaotic attractor. It is worth noting that quasi-periodic and chaotic windows look similar in bifurcation diagrams in Fig. 12, and only further analysis via Poincaré maps and Lyapunov exponents can shed light on the exact type of system oscillations. The systems chaotic behavior, as observed in the results, is validated by the variation of the largest Lyapunov exponent λ_1 with respect to the number of forcing periods n , as illustrated in Fig. 20.

5 Conclusion

This paper presents a thorough analytical and numerical investigation of the detailed complex dynamic behavior of a nonlinear two-degree-of-freedom parametric oscillator that includes dry friction, magnetic stiffness, and time-periodic coupling from a rectangular cross-section rotating beam. The extension of earlier published work [48, 49] 1DOF models to a more representative coupled system effectively captured the interaction of nonlinear restoring forces and nonsmooth friction dynamics. Analytical solutions derived from the Complex Averaging method have been validated by numerical solutions, demonstrating a variety of dynamical regimes, including periodic, quasi-periodic, and chaotic responses. We have plotted the Lyapunov exponents to explore the behavior of the system's motion. Lyapunov exponents provide a measure of how small differences in initial conditions evolve over time. They help identify whether the system settles into regular or chaotic motion. This makes them a valuable tool for understanding the stability of complex dynamic systems. The system behaves similarly to the 1DOF case for the case of different masses, while it displays complex bifurcation patterns and multistability, which are significantly affected by the order of nonlinear stiffness, friction intensity, and mass arrangement. These findings enhance the theoretical comprehension of coupled nonlinear oscillators with nonsmooth properties and establish a solid basis for practical applications. The insights acquired are pertinent to the advancement of efficient vibration control systems, nonlinear energy harvesters, and complicated mechanical structures that utilize multistable and resonance-enhanced dynamics.

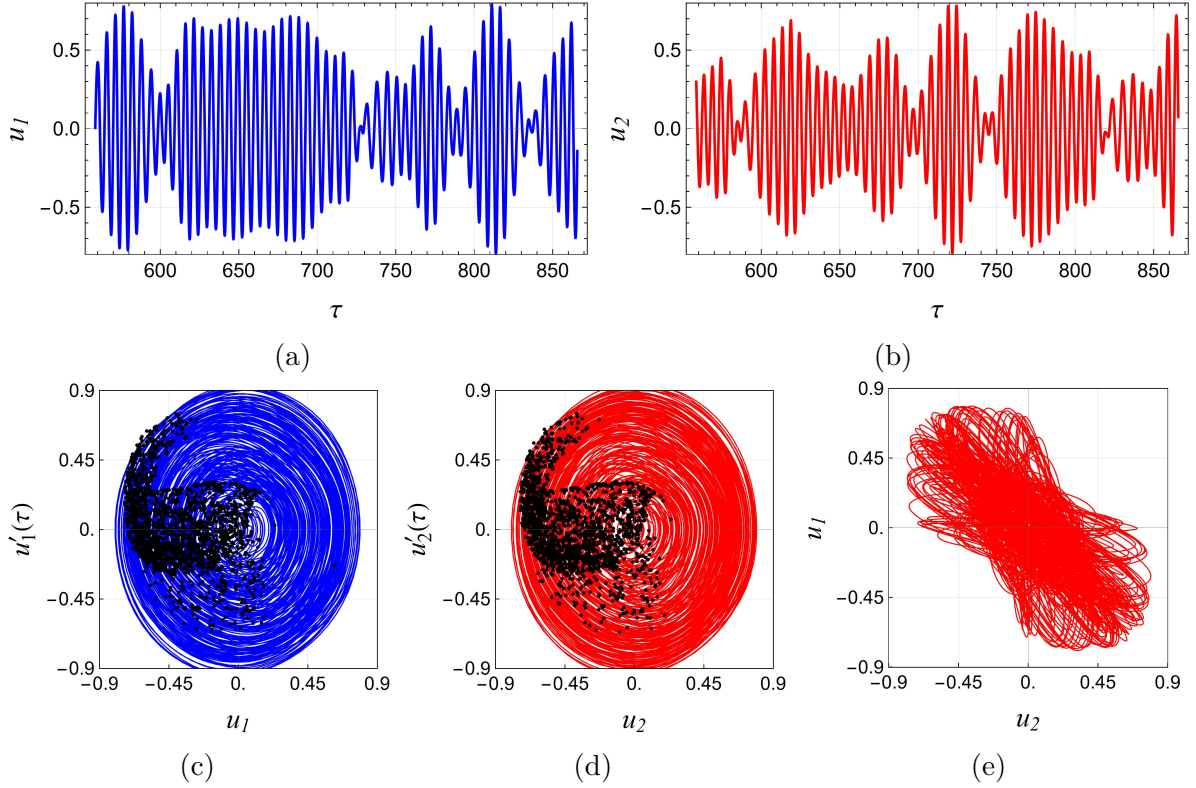


Figure 19: The time-domain plots (top) show near steady-state oscillations for u_1 and u_2 after an initial transient phase of 100 periods, $\omega = 1.125$. The phase-space plots (bottom) display an uncertain trajectory, and the Poincaré section indicates a chaotic regime.

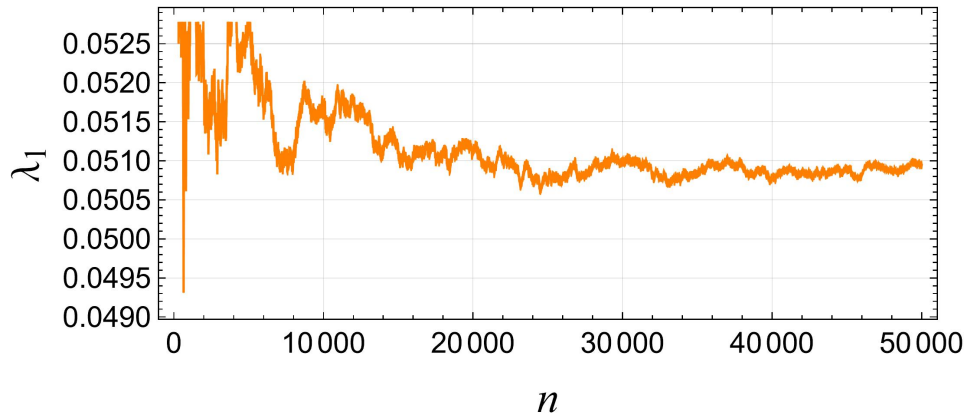


Figure 20: The maximal Lyapunov exponent λ_1 as a function of the number of external forcing periods n for $\omega = 1.125$

Future work the complexity and richness of the observed dynamics motivate further analytical, numerical, and experimental efforts. Building on the present CxAnumerical framework, our next planned research will focus on the application of additional semi-analytical techniques, such as the Method of Multiple Scales (MMS) for capturing slowfast dynamics and the Harmonic Balance Method (HBM) for accurately predicting periodic and quasi-periodic responses. We have already successfully applied MMS and HBM to our earlier published work, a 1DOF parametric oscillator with dry friction [49]. On the numerical side, advanced continuation algorithms and basin-of-attraction mapping will be employed to explore global bifurcations and hidden attractors. Furthermore, experimental validation using an extended version of the 1DOF setup to a full 2DOF configuration is a key objective, enabling direct comparison of theoretical predictions with real-world behavior.

Author contribution statement

Muhammad Junaid-U-Rehman: Conceptualization, Investigation, Methodology, Validation, Software, Visualization, WritingOriginal draft **Grzegorz Kudra:** Conceptualization, Methodology, Validation, Software, Visualization, WritingReviewing and Editing, Supervision, Project Administration; **Krystian Polczyski:** Investigation, Data Curation, Validation, Software; **Kevin Dekemele:** Investigation, Methodology, Software, Formal analysis; **Jan Awrejcewicz:** Supervision, Formal Analysis.

Acknowledgements

This research has received funding from the National Science Center, Poland, under the grant PRELUDIUM 23 No. DEC-2024/53/N/ST8/00400. This article was completed while the first author, Muhammad Junaid-U-Rehman, is a PhD student at the Interdisciplinary Doctoral School of Lodz University of Technology, Poland. For the purpose of Open Access, the authors have applied a CC-BY public copyright license to any Author Accepted Manuscript (AAM) version arising from this submission.

Declaration of competing interest

The authors affirm that no personal relationships or recognized competing financial interests could have influenced the research provided in this study.

Data availability

Data will be provided upon request.

References

- [1] Awrejcewicz, J. (2014), Ordinary differential equations and mechanical systems, [Click URL](#).
- [2] Fucik, S., & Kufner, A. (2014). Nonlinear differential equations (Vol. 2). Elsevier, [Click URL](#).

- [3] Awrejcewicz, J. (2012) Bifurcation and chaos: theory and applications. Springer Science and Business Media, [Click URL](#).
- [4] Fertis, D. G. (1998). Nonlinear mechanics. CRC press, [Click URL](#).
- [5] Ramaswamy, J. (2025). Applications of Differential Equations. Educohack Press, [Click URL](#).
- [6] Benacchio, S., Giraud-Audine, C., Thomas, O. (2022) Effect of dry friction on a parametric nonlinear oscillator, *Nonlinear Dynam.* 108 (2) 1005 – 1026, [Click URL](#).
- [7] M. Aghamohammadi, M., Sorokin, V., Mace, B. (2019) On the response attainable in nonlinear parametrically excited systems, *Appl. Phys. Lett.*, 115(15), 154102, [Click URL](#).
- [8] Azimi, M. (2022) Stability and bifurcation of Mathieu-Duffing equation, *International Journal of Non-Linear Mechanics*, 144, 104049, [Click URL](#).
- [9] Barakat, A.A., Weig, E.M., Hagedorn, P. (2023) Non-trivial solutions and their stability in a two-degree-of-freedom Mathieu-Duffing system, *Nonlinear Dyn*, 111 : 22119, 22136, [Click URL](#).
- [10] Sani, G., Balaram, B., Awrejcewicz, J. (2023). Nonlinear interaction of parametric excitation and self-excited vibration in a 4 DoF discontinuous system, *Nonlinear Dyn*, 111 2203 – 2227, [Click URL](#).
- [11] Thomsen, J.J. (2003). Vibrations and Stability: Advanced Theory, Analysis, and Tools, ed Springer, Berlin, New York, [Click URL](#).
- [12] Bartuccelli, M.V., Gentile, G., Georgiou, K.V. (2016). On the dynamics of a vertically driven damped planar pendulum, *Proc. R. Soc. A Math. Phys. Eng. Sci.* 457 3007 – 3022, [Click URL](#)
- [13] Craninckx, J., and Steyaert, M. (1995). "Low-noise voltage-controlled oscillators using enhanced LC-tanks," in *IEEE Transactions on Circuits and Systems II: Analog and Digital Signal Processing*, 42 (12) 794 – 804, [Click URL](#).
- [14] Juraschek, D.M., Meier, Q.N., Narang, P. (2020). Parametric Excitation of an Optically Silent Goldstone-Like Phonon Mode, *Physical review letter*, 124, 117401, [Click URL](#)
- [15] Butikov, E.I. (2011) An improved criterion for Kapitzas pendulum stability, *J. Phys. A Math. Theor.* 44 (29) 295202, [Click URL](#).
- [16] Nayfeh, A. H., & Mook, D. T. (2024). Nonlinear oscillations. John Wiley & Sons, [Click URL](#).
- [17] Nayfeh, A.H. (2024). Perturbation methods. John Wiley & Sons, [Click URL](#).
- [18] Nayfeh, A. H. (2005). Resolving controversies in the application of the method of multiple scales and the generalized method of averaging. *Nonlinear Dynamics*, 40, 61-102, [Click URL](#).

- [19] J. Awrejcewicz, R. Starosta, and G. Sypniewska-Kamiska. Asymptotic multiple scale method in time domain: Multi-Degree-of-Freedom stationary and nonstationary dynamics, CRC Press, 2022, [Click URL](#).
- [20] Bowden, F. P., & Tabor, D. (2001). The friction and lubrication of solids (Vol. 1). Oxford University Press. [Click URL](#).
- [21] Karnopp, D. (1985). Computer simulation of stick-slip friction in mechanical dynamic systems. *Journal of Dynamic Systems, Measurement, and Control*, 107(1), 100-103, [Click URL](#).
- [22] Filippov, A. F. (2013). Differential equations with discontinuous righthand sides: control systems (Vol. 18). Springer Science & Business Media, [Click URL](#).
- [23] Armstrong-Helouvry, B. (1991). Control of machines with friction (Vol. 128). Springer Science & Business Media, [Click URL](#).
- [24] Haessig Jr, D. A., & Friedland, B. (1991). On the modeling and simulation of friction, [Click URL](#).
- [25] De Wit, C. C., Olsson, H., Astrom, K. J., & Lischinsky, P. (1995). A new model for control of systems with friction. *IEEE Transactions on automatic control*, 40(3), 419-425, [Click URL](#).
- [26] Shaw, S. W. (1986). On the dynamic response of a system with dry friction. *Journal of Sound and Vibration*, 108 (2), 305-325, [Click URL](#).
- [27] Awrejcewicz, J., & Delfs, J. (1990). Dynamics of a self-excited stick-slip oscillator with two degrees of freedom. I, Investigation of equilibria. *European Journal of Mechanics. A. Solids*, 9 (4), 269-282, [Click URL](#).
- [28] Feeny, B., & Moon, F. C. (1994). Chaos in a forced dry-friction oscillator: Experiments and numerical modeling. *Journal of Sound and Vibration*, 170 (3), 303-323, [Click URL](#).
- [29] Oestreich, M., Hinrichs, N., & Popp, K. (1996). Bifurcation and stability analysis for a non-smooth friction oscillator. *Archive of Applied Mechanics*, 66, 301-314, [Click URL](#).
- [30] Armstrong-Hélouvry, B., Dupont, P., & De Wit, C. C. (1994). A survey of models, analysis tools and compensation methods for the control of machines with friction. *Automatica*, 30(7), 1083-1138, [Click URL](#).
- [31] Hoffmann, N., & Gaul, L. (2003). Effects of damping on mode-coupling instability in friction-induced oscillations. *ZAMMJournal of Applied Mathematics and Mechanics/Zeitschrift für Angewandte Mathematik und Mechanik: Applied Mathematics and Mechanics*, 83 (8), 524534, [Click URL](#).
- [32] Fritz, G., Sinou, J. J., Duffal, J. M., & Jézéquel, L. (2007). Effects of damping on brake squeal coalescence patternsapplication on a finite element model. *Mechanics Research Communications*, 34 (2), 181-190, [click URL](#).

- [33] Sinou, J. J., & Jézéquel, L. (2007). Mode coupling instability in friction-induced vibrations and its dependency on system parameters including damping. *European Journal of Mechanics-A/Solids*, 26, 106-122, [Click URL](#).
- [34] Massi, F., & Giannini, O. (2008), Slight effect of damping on the propensity of squeal instability: An experimental investigation. *The Journal of the Acoustical Society of America*, 123(4), 2017-2023. [Click URL](#).
- [35] Charroyer, L., Chiello, O., & Sinou, J. J. (2016). Parametric study of the mode coupling instability for a simple system with planar or rectilinear friction. *Journal of Sound and Vibration*, 384, 94-112. [Click URL](#).
- [36] Li, Z., Ouyang, H., & Guan, Z. (2016). Nonlinear friction-induced vibration of a sliderbelt system. *Journal of Vibration and Acoustics*, 138 (4), 041006, [Click URL](#).
- [37] Cveticanin, L. (2001). Vibrations of a coupled two-degree-of-freedom system. *Journal of Sound and Vibration*, 247 (2), 279-292, [Click URL](#).
- [38] Vakakis, A. F., & Rand, R. H. (2003, January). Nonlinear dynamics of a system of coupled oscillators with essential stiffness nonlinearities. In *International Design Engineering Technical Conferences and Computers and Information in Engineering Conference* (Vol. 37033), [Click URL](#).
- [39] Kudra, G.; Witkowski, K. Seth, S. Polczyski, K. Awrejcewicz, J. Parametric Vibrations of a System of Oscillators Connected with Periodically Variable Stiffness. In *Proceedings of the DSTA-2021 Conference BooksAbstracts (16th International Conference: Dynamical Systems Theory and Applications DSTA 2021 ABSTRACTS)*, ódz, Poland, 1619 December 2021, Wydawnictwo Politechniki ódzkiej, Awrejcewicz, J., Kazmierczak, M., Olejnik, P., Mrozowski, J., Eds.; ISBN 978 – 83 – 66741 – 20 – 1. [Click URL](#).
- [40] Dimarogonas, A.D., and Haddad, S. (1992). *Vibration for Engineers*, Prentice-Hall, Englewood Cliffs, New Jersey, [Click URL](#).
- [41] Dimarogonas, A.D., (1996). *Vibration for Engineers*, Prentice-Hall, Englewood Cliffs, NJ, [Click URL](#).
- [42] Hagedorn, P., Schwingungen, N., (1978). *Akademische Verlagsgesellschaft*, Wiesbaden, [Click URL](#).
- [43] Nayfeh, A.H., Mook, D.T., (1979). *Nonlinear Oscillations*, Wiley, New York, [Click URL](#).
- [44] Krack, M., & Gross, J. (2019). Harmonic balance for nonlinear vibration problems (Vol. 1, pp. 26-28). Cham: Springer, [Click URL](#).
- [45] Awrejcewicz, J., Kudra, G., & Mazur, O. (2021). Double-mode model of size-dependent chaotic vibrations of nanoplates based on the nonlocal elasticity theory. *Nonlinear Dynamics*, 104 (4), 3425-3444, [Click URL](#).

[46] Awrejcewicz, J., Kudra, G., & Mazur, O. (2025). Stability and bifurcation analysis of simply supported rectangular nanoplate embedded on visco-Pasternak foundation based on first-order shear deformation theory. *Composite Structures*, 354, 118728, [Click URL](#).

[47] Awrejcewicz, J., Kudra, G., & Mazur, O. (2023). Chaotic vibrations of double-layer graphene sheet system. *International Journal of Non-Linear Mechanics*, 157, 104538, [Click URL](#).

[48] G. Kudra, K. Witkowski, A. Fasihi, G. Wasilewski, S. Seth, K. Polczyski, J. Awrejcewicz, Bifurcation dynamics of a 1DOF parametric oscillator with stiffness-hardening characteristic and dry friction. *Journal of Sound and Vibration*, 543 (2023) 117356, [Click URL](#).

[49] M. Junaid-U-Rehman, G Kudra, K. Witkowski, G. Wasilewski, F. Jarad, J. Awrejcewicz, Analytical, numerical, and experimental observation of isolated branches of periodic orbits in 1DOF mechanical parametric oscillator. *Journal of Sound and Vibration*, 584 (2024) 118454, [Click URL](#).

[50] Huang, L., & Yang, X. D. (2023). Dynamics of a novel 2-DOF coupled oscillators with geometry nonlinearity. *Nonlinear Dynamics*, 111(20), 18753-18777, [Click URL](#).

[51] Chen, P., & Yang, X. D. (2025). Dynamics analysis of a bistable 2-DOF coupled oscillator with nonlinear damping. *International Journal of Non-Linear Mechanics*, 105021, [Click URL](#).

[52] Dekemele, K., Giraud-Audine, C., & Thomas, O. (2024). A piezoelectric nonlinear energy sink shunt for vibration damping. *Mechanical Systems and Signal Processing*, 220, 111615, [Click URL](#).

[53] Gendelman, O. V. (2011). Targeted energy transfer in systems with external and self-excitation. *Proceedings of the Institution of Mechanical Engineers, Part C: Journal of Mechanical Engineering Science*, 225 (9), 2007-2043, [Click URL](#).

[54] Manevitch, L. (2001). The description of localized normal modes in a chain of nonlinear coupled oscillators using complex variables. *Nonlinear Dynamics*, 25, 95-109, [Click URL](#).

[55] Bitar, D., Ture Savadkoohi, A., Lamarque, C. H., Gourdon, E., & Collet, M. (2020). Extended complexification method to study nonlinear passive control. *Nonlinear Dynamics*, 99, 1433-1450, [Click URL](#).

[56] Habib, G., & Romeo, F. (2021). Tracking modal interactions in nonlinear energy sink dynamics via high-dimensional invariant manifold. *Nonlinear Dynamics*, 103(4), 3187-320, [Click URL](#).